Materials Science & Engineering A 941 (2025) 148410

Contents lists available at ScienceDirect

Materials Science & Engineering A

journal homepage: www.elsevier.com/locate/msea

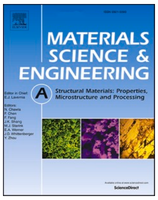

Elastic moduli of 6th generation Ni-base single crystal superalloy TMS-238 and its tie-lined γ and γ' phases

Takuma Saito[a,*,1], Hiroshi Harada[a,2], Makoto Osawa[a], Tadaharu Yokokawa[a], Kyoko Kawagishi[a,b], Shinsuke Suzuki[b]

[a] National Institute for Materials Science, 1-2-1 Sengen, Tsukuba, 305-0047, Ibaraki, Japan
[b] Waseda University, 3-4-1 Okubo, Shinjuku-ku, Tokyo, 169-8555, Japan

ARTICLE INFO

Keywords:
Superalloy
Elastic modulus
Composite model
Resonance method
Tie-lined alloys
Single crystal
Raft structure

ABSTRACT

Understanding the precise elastic modulus of individual γ and γ' phases is crucial for estimating the elastic misfit between these phases, because it is a key factor in controlling the formation of raft structures and local stress/strain around γ' precipitates. Despite its importance, research in this area remains limited. This study determines the elastic modulus of 6th generation Ni-base single crystal superalloy TMS-238 and its tie-lined γ and γ phases under equilibrium conditions above 900 °C. We fabricated TMS-238 and its tie-lined alloys with varying γ' volume fractions. Using the rectangular parallelepiped resonance (RPR) method, we measured the elastic modulus from room temperature to 1100 °C. Elastic moduli between tie-lined phases were then estimated above 900 °C using composite models. Our findings were compared with those of Ni-Al binary alloys, Ni-Al-X ternary alloys, and multi-component systems, providing a comprehensive understanding of the elastic properties.

1. Introduction

Ni-base single-crystal superalloys, which usually consist of cubic γ' precipitates based on $L1_2$ structure and γ matrix based on FCC solid solution, are used as a material for components in the hot section of gas turbine systems for power generators and jet engines [1–3]. Among the components, turbine blades are well known for their critical role in determining the efficiency of the systems.

Coherent γ/γ' interface plays a key role as an important strengthening mechanism [4–6], and the coherent loss on the γ/γ' interface accelerates creep deformation [7,8]. The coherent interface is a source of local stresses/strains which prevents dislocations from moving [9,10] and which causes raft structure formation during creep at lower stress and higher temperature conditions [11–16], due to a difference of physical parameters between the γ and γ' phases [17–25] with enough high diffusivity of alloying elements [26,27]. Therefore, alloy design to realize larger negative lattice misfit between the γ and γ' phases, defined by $\delta_L = \frac{a_{\gamma'} - a_\gamma}{a_\gamma}$ where a is lattice constant, has been performed to obtain higher temperature durability [28], which is different from the alloy design strategy in intermediate temperature range without raft structure formation [29,30]. It is well known that negatively larger lattice misfit tends to realize dislocation network with finer spacing [31] and form larger perfection degree of the raft structure [32], which could contribute to superior creep resistance at lower stress and higher temperature conditions. However, above mentioned equation of the lattice misfit does not reflect the correct view of lattice misfit during the loading because the elastic misfit between the phases, defined by $\delta_E = \frac{E_{\gamma'} - E_\gamma}{E_\gamma}$ where E is <100> longitudinal elastic modulus, have to be taken into account. Considering the elastic misfit, the lattice misfit on vertical γ/γ' interface is modulated to $\delta^V_{t-E,L} = \left\{(1+\delta_L)\left(\frac{\sigma_{ext}}{E_{\gamma'}}+1\right) - \left(\frac{\sigma_{ext}}{E_\gamma}+1\right)\right\}\Big/\left(\frac{\sigma_{ext}}{E_\gamma}+1\right)$, and that on horizontal γ/γ' interface is modulated to $\delta^H_{t-E,L} = \left\{(1+\delta_L)\left(-\frac{\nu_{\gamma'}\cdot\sigma_{ext}}{E_{\gamma'}}+1\right) - \left(-\frac{\nu_\gamma\cdot\sigma_{ext}}{E_\gamma}+1\right)\right\}\Big/\left(\frac{\nu_\gamma\cdot\sigma_{ext}}{E_\gamma}+1\right)$ [33] in the case of conventional superalloys with negative lattice misfit under uniaxial tensile load. Such misfit during the loading is called "true misfit" [33] which is a driving force for the rafting, and causes local strain/stress field around γ' precipitates [17]. Therefore, the elastic

---

* Corresponding author.
E-mail address: Takuma.Saito@ruhr-uni-bochum.de (T. Saito).

[1] Present address: Ruhr-University Bochum, Universitätsstraße 150, 44801 Bochum, Nordrhein-Westfalen, Germany

[2] Present address: Superalloys Design Laboratory, 3-18-33 Azuma, Tsukuba, 305-0031, Japan.

https://doi.org/10.1016/j.msea.2025.148410
Received 18 January 2025; Received in revised form 5 April 2025; Accepted 26 April 2025

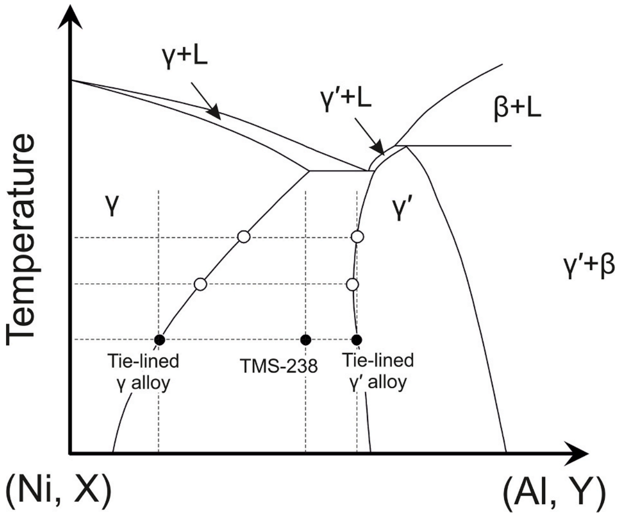

Fig. 1. Concept of the tie-lined alloys in pseudo-binary phase diagram.

misfit seems to have a key for novel alloy design approach [34]. For instance, positively larger elastic misfit contributes to larger driving force for the raft structure formation, resulting in positive effect on creep lives [33,34].

Estimating the elastic misfit at higher temperatures is significant for novel alloy design of superalloys [33]. A problem in this situation is that it is significantly difficult to measure the elastic misfit from one specimen consisting of γ' precipitates and γ matrix. Therefore, a solution to assume the elastic modulus of the individual γ and γ' phases is to measure the elastic modulus using alloys with individual single phases, which are equilibrium at specified temperature ranges [35,36]. This approach is ideal to assume the elastic modulus of the alloy system at specified temperature, however, most of previous efforts has been conducted with simple alloy systems such as Ni-Al-Mo: R1/R2 alloys for a range between 1000 and 1050 °C, and R3/R4 alloys for a range between 950 and 1000 °C [37]. Designing alloys with γ or γ' single phase alloy in multi-component systems is difficult due to lack of equilibrium information of microstructure. For instance, previous research to determine the elastic misfit of superalloys, CMSX-4 with multi-component systems, uses modeled alloys with individual γ and γ' phases, in addition to CMSX-4 with both γ and γ' phases itself [36,38,39]. In that research, the modeled alloy with γ single phase does not contain any γ' former element of Al, Ti, Ta, and Hf ($Ni_{54.9}Co_{18.6}Cr_{20}Mo_{0.8}W_{2.7}Re_3$ (at.%)), furthermore, the modeled alloy with γ' single phase also does not contain any γ former element of Cr, Cr, W, Mo, and Re ($Ni_{75}Al_{23}Ti_2Ta_1$ (at.%)) to ensure the alloys with single phases. In another case of Mar-M002 mod, the modeled alloy with γ single phase is $Ni_{81}Co_{5.8}Cr_{9.9}W_{3.3}$ (at.%), and that with γ' single phase is $Ni_{72.5}Al_{26.5}$ (at.%) [40]. However, equilibrium compositions of γ' phase actually contains γ former elements, and those of γ phase also contain γ' former elements [41,42], that is different situation of the modeled alloys with individual phases in previous research.

National Institute for Materials Science (NIMS) in Japan can precisely predict the equilibrium compositions of individual γ and γ' phases in superalloys because NIMS has developed Alloy Design Program (ADP) for over 50 years which is using in-house database of microstructure and properties [43]. Using ADP, we can fabricate a series of equilibrium alloys with individual phase (so called, tie-lined alloys) shown in Fig. 1. We measured their elastic modulus, and established the predictive equations of the elastic modulus of γ or γ' single phases to estimate the elastic modulus in a function of compositions and temperatures [35]. While our primary focus has been on the tie-lined alloys with single phase, it is also essential to evaluate the elastic properties of multi-component two-phase superalloys for practical applications. Such data are also significantly valuable for validating the elastic properties of the tie-lined alloys using composite models [36–38]. Furthermore, the concept of "tie-lined alloys" are basically referred to the alloys with the equilibrium compositions at specified temperatures. Therefore, when discussing elastic misfit between phases at elevated temperatures, it is important to consider the temperature dependence of equilibrium compositions, even above the temperatures at which the tie-lined alloys are defined, as illustrated in Fig. 1.

Based on these backgrounds, this manuscript aims to determine the elastic properties mainly focusing on <001> longitudinal elastic modulus, which is necessary for the estimation of the elastic misfit, of 6th generation Ni-base single-crystal superalloy in multi-component systems, TMS-238 [44], using Rectangular Parallelepiped Resonance (RPR) method [45–47], at elevated temperatures. For the estimation of the elastic misfit based on equilibrium compositions of each phase, tie-lined alloys of the individual γ and γ' phases were fabricated and used in addition to original TMS-238.

2. Procedure

Compositions of the individual γ and γ' phase alloys in equilibrium condition at 900 °C were determined using Alloy Design Program (ADP) [43] with original TMS-238 [44]. Table 1 shows the compositions of TMS-238 and its equilibrium compositions in individual γ and γ' phases at 900, 1000, and 1100 °C. These designed compositions were compared with reference values of the individual phases measured by experiments in Table 1. Compositions of the individual γ and γ' phases were measured by electron probe micro-analyzer (EPMA: Shimadzu EPMA-1610) at 15 kV of accelerate voltage and 20 nA of beam current size with 50 µm of beam size using TMS-238 with strain aged at 900 °C for 1500 h and at 1100 for 500 h, and the measured are almost identical to those

Table 1
Compositions of TMS-238 and its equilibrium compositions of the individual phases (at.%), Ni: bal. Exp.* indicates EPMA analysis on single crystal specimens after heat treatment, Exp. ** indicates EPMA analysis on strain-aged specimens.

Alloys	T/°C		Co	Cr	Mo	W	Al	Ta	Hf	Re	Ru	Designed $V_{\gamma'}$
TMS-238	900	ADP	7.0	5.6	0.7	1.4	13.9	2.7	0.04	2.2	3.1	0.72
	1000											0.69
	1100											0.62
	–	Exp.*	7.0	5.2	0.8	1.2	13.1	2.8	0.04	2.4	3.5	–
Tie-lined γ phase	900	ADP	12.5	14.3	1.4	1.6	5.0	0.8	0.01	6.3	5.7	0.00
		Exp.**	10.0	12.3	2.6	1.9	4.2	0.6	0.01	5.9	6.6	
	1000	ADP	11.1	12.5	1.4	1.6	6.5	1.0	0.01	5.4	5.0	
	1100	ADP	9.8	10.5	1.3	1.6	8.3	1.3	0.01	4.4	4.3	
		Exp.**	9.6	9.6	1.2	1.8	8.4	1.3	0.04	4.6	5.0	
Tie-lined γ' phase	900	ADP	4.8	2.2	0.5	1.3	17.3	3.4	0.05	0.6	2.1	1.00
		Exp.**	3.5	2.1	1.1	1.5	17.0	3.1	0.07	0.4	1.5	
	1000	ADP	5.2	2.5	0.4	1.3	17.2	3.4	0.05	0.7	2.3	
	1100	ADP	5.3	2.6	0.4	1.2	17.3	3.5	0.05	0.8	2.4	
		Exp.**	5.0	2.4	0.5	1.2	17.1	3.9	0.07	0.5	2.1	

Table 2

Single crystalline specimens of TMS-238 and its tie-lined γ and γ′ phase alloys for RPR method.

Alloys	Average length			Weight *g*	Density *g/mm*^{3}
	x /*mm*	y /*mm*	z /*mm*		
TMS-238	4.8460	4.7445	4.5775	0.94952	9022.01
Tie-lined γ phase alloy	3.7518	4.0688	4.0483	0.60030	9873.52
Tie-lined γ′ phase alloy	4.0985	4.0985	3.9593	0.57694	8674.92

calculated by ADP. This result indicates that the alloy design by ADP is reasonable.

Single-crystals of the tie-lined Ni-base superalloy TMS-238 (tie-lined γ phase alloy, original TMS-238 with γ and γ′ phases, and tie-lined γ′ phase alloy) were fabricated using a directionally solidified furnace at vacuum atmosphere. Raw materials of TMS-238 were melted in Al_2O_3 crucible heated at 1600 °C, then the molten metal was poured into a casting mold having eight cylindrical parts. The mold has a diameter of 11 mm and longitudinal length of 140 mm with a pig-tail typed grain-selectors, and the mold was kept at 1550 °C. Next, the mold was pulled down at 200 mm/h into the cooling chamber of the furnace. After the casting, the same heat treatments consisting of solution (1300 °C/1 h → 10 min → 1310 °C/1 h → 60 min → 1335 °C/5 h → 60 min → 1345 °C/20 h), primary aging (1150 °C/2 h) and secondary aging (870 °C/20 h) shown in Table 2 were applied to each as-cast metal in vacuum furnace. After each heat treatment step, the cast metal was cooled under vacuum. Then, rods of single-crystals whose crystal orientation along longitudinal direction is almost [001] were obtained by breaking the mold and cutting the metals using a precision cutting machine (HS-100, HEIWA TECHINCA, Tokyo, Japan). Microstructure after the heat treatments was observed using a field-emission type scanning electron microscope (JEM-7200. JEOL, Tokyo, Japan) at 20 kV. Additionally, the composition of TMS-238 single crystal after heat treatment was measured by EPMA with 50 μm of beam size to analyze alloy compositions, and the result is shown in Table 1.

Rod-like single crystals were machined into rectangular parallelepiped specimens with {100} crystal orientations on each surface. The crystal orientation was determined using the X-ray back-reflection Laue

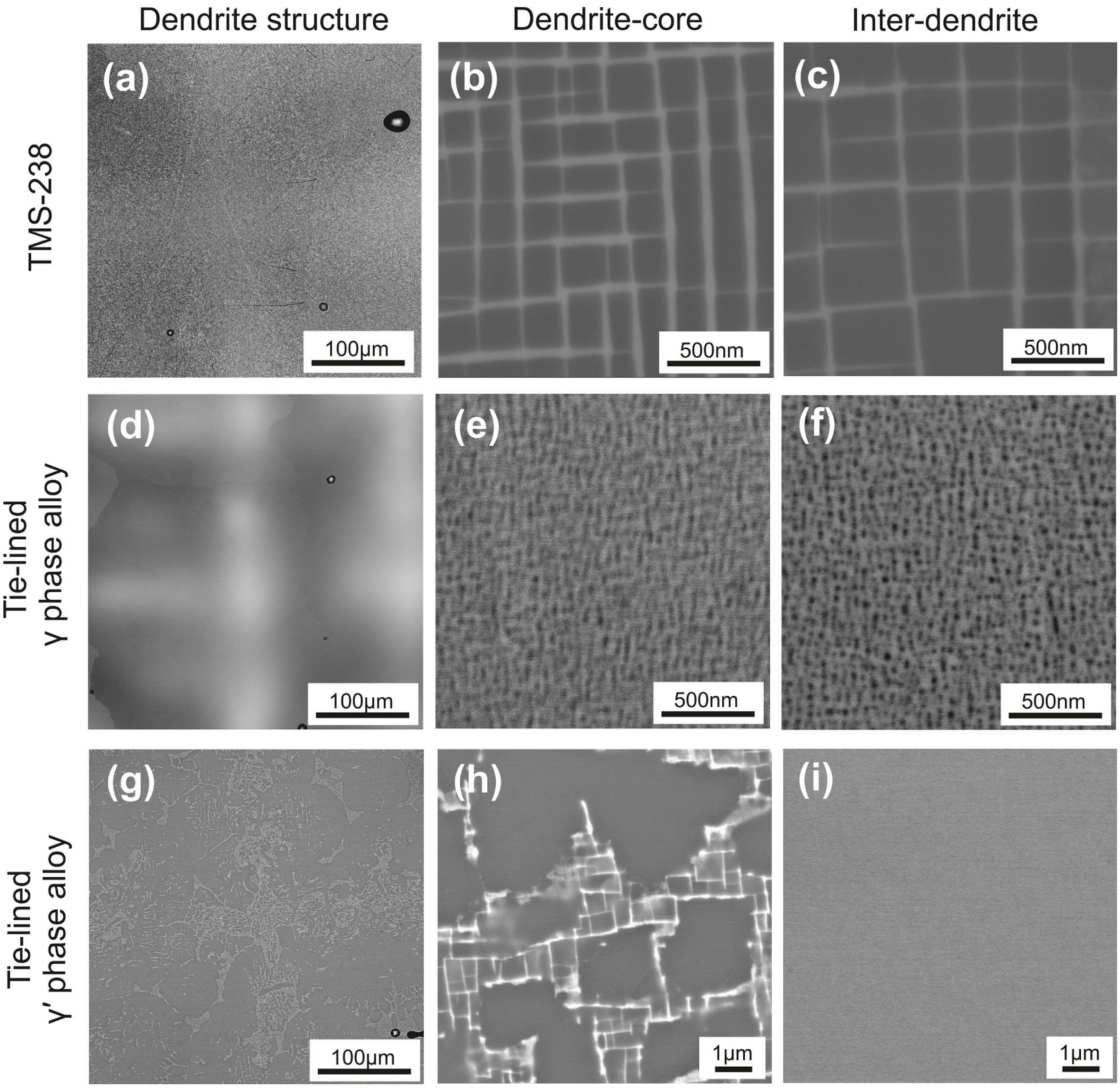

Fig. 2. Microstructure of TMS-238 and its tie-lined phase alloys.
(a-c) TMS-238, (d–f) tie-lined γ phase alloy, (g–i) tie-lined γ′ phase alloy,
(a, d, g) dendritic strcture, (b, e, h) dendrire core region, and (c, f, i) inter dendrite region.

method with an X-ray generator (SA-HF3, Rigaku, Tokyo, Japan), and cutting was performed using a wire EDM machine (HS-300, BROTHER INDUSTRIES, LTD., Aichi, Japan). After this process, further precision machining was carried out to improve the parallelism of opposite faces and to accurately control the dimensions of each edge, as described below. One of the planes whose crystal orientation was aligned to be <100> by Laue method was attached to a sample holder with a 2-axis goniometer (M − 127, SERVTEC Co. Ltd., Chiba, Japan). The surface opposite to the initially attached face was polished using 30-μm diamond slurry and lapping plate, ensuring the {111} plane was accurately exposed. Subsequently, The polished surface was then mounted onto another sample holder (M − 6325, SERVTEC Co. Ltd., Chiba, Japan). The surface opposite to the newly attached face was subsequently polished to expose the {100} plane. This polishing procedure was repeated three times to ensure that precise {100} planes were exposed on all faces of the specimen. It should be noted that polishing was performed to produce rectangular parallelepiped specimens, rather than perfect cubes, in order to sufficiently separate resonance frequencies for in the following analysis. As a result, specimens with approximate edge lengths of 4 mm and surfaces nearly parallel to the {100} planes were fabricated. The edge lengths and weights of the specimens were then precisely measured using a micrometer and an electronic balance, respectively.

Subsequently, average edge lengths in each direction were calculated, and the specimen volumes were determined based on these averages, assuming an ideal rectangular parallelepiped shape. The densities were then calculated by dividing the measured weight by the calculated volume. The details of the specimens are summarized in Table 2.

To obtain the elastic modulus of the specimens, rectangular parallelepiped resonance (RPR) method [46–48] was used. RPR method consist of two steps, experimental and simulation parts, respectively. In the experiment, resonance spectrum of the specimen was obtained at 1.0×10^{-4} Pa, from room temperature to 1100 °C, using an RPR apparatus (CC-HT, Japan Techno Plus Co. Ltd., Osaka, Japan). Range of frequency was between 250 and 1250 kHz during the experiment. During the measurement of resonance frequency, the target temperature is kept for approximately 30 min. In the simulation, spectrum of the resonance frequency of the specimens consisting of OD, EV, OX, OY, OZ, EX, EY and EZ resonance modes from 1st to 8th degree was simulated by assuming the elastic moduli c_{11}, c_{12}, and c_{44} in FCC lattice, inputting density, and edge length of the specimen, using a software program (f-calc ™, Japan Techno Plus Co. Ltd., Osaka, Japan). The simulation was repeated to fit experimental one until the degree of coincidence between the measured spectra $f_{i,j}^{mea}$ and simulated spectra $f_{i,j}^{sim}$ about i-th resonance frequency of j-mode shown in Equation (1) was smaller than 0.5 %.

$$S = \sum_{j}\sum_{i}\left(\frac{f_{i,j}^{sim} - f_{i,j}^{mea}}{f_{i,j}^{sim}}\right) \tag{1}$$

3. Results

3.1. Microstructure of specimens

Fig. 2 shows microstructure of the alloys. All alloys have inhomogeneous microstructure in dendritic scales, originating from solidification process [49]. Dendritic shape was confirmed in each alloy shown in Fig. 2(a), 2(d) and 2(g), indicating that elemental segregation caused during solidification remains after the heat treatments.

In the case of γ+γ' alloy TMS-238 shown in Fig. 2 (b) and 2 (c), cubic and aligned γ' precipitates with darker contrast are surrounded by thin γ matrix channels with brighter contrast in back scattered electron images. The edge length of the γ' precipitates tends to be larger in the inter-dendrite region than that in the dendrite-core region. This difference originates from dendritic scaled segregation of heavy elements such as W and Re during solidification process. As the result of segregated W and Re in the dendrite core region which is remained after solution treatment, these heavy elements retard growth of the γ' precipitates in the dendrite core region more than the inter dendrite region during primary aging [50].

In the case of tie-lined γ phase alloy shown in Fig. 2(e) and 2 (f), black contrasted tiny precipitates with approximately 10 nm in a diameter were found to be distributed homogenously and monomodally between the dendrite core and the inter dendrite regions, respectively. Since darker contrast in BSE images implies the existence of lighter elements, these darker contrasted regions indicate the γ' precipitates. Since tie-lined γ phase alloy was designed to be equilibrium at 900 °C with γ' precipitates, this alloy has γ and γ' phases in equilibrium state enough below 900 °C if solvus line of γ phase with γ and γ' coexisted region in TMS-238 follows Ni-Al alloy system in phase diagram. Notably, the tie-lined γ phase alloy is pure γ phase above 900 °C since the dissolubility of γ' former elements such as Al and Ta in γ phase increases with increase of temperature [41,42]. Therefore, observed tiny and monomodal γ' precipitates are formed during cooling process, but not during aging. If these tiny γ' precipitates have already appeared during primary and secondary aging, multi-modal distribution of γ' precipitates would be observed due to cooling γ' precipitate formed during cooling process in addition to grown γ' precipitates formed during the final aging. From these observed points, the tie-lined γ phase alloy is expected to show a pure γ phase approximately above 900 °C.

In the case of tie-lined γ' phase alloy shown in Fig. 2 (h) and 2 (i), fine network consisting of thin γ matrix channels with brighter contrast was observed, especially in the dendrite core region. This observation indicates that γ former element is more distributed in dendrite core region during the solidification process, and this segregation remains after solution treatment. Furthermore, γ phase in the tie-lined γ' phase alloy can be supposed to appear during cooling process from solidification and solution treatment. The γ' precipitates surrounded by γ channel grow during primary aging at 1150 °C with high influence from the lattice misfit [51] since γ' precipitates with aligned and cubic shape appear with thin γ channels especially in the dendrite core region. In this estimation, γ phase also appears and continues to grow with γ' precipitates in the secondary aging at 870 °C. Therefore, existence of the γ phase in the tie-lined γ' phase alloy cannot be ignored to consider the elastic modulus of pure γ' phase even over the temperature of secondary aging 870 °C, which is a different case from that of the tie-lined γ phase alloy. Notably, according to Ni-Al phase diagram [52] and temperature dependence of compositions in equilibrium phases of superalloys [41,42], composition of the γ' phase does not change significantly as temperature changes. Therefore, the volume fraction of γ phase in the tie-lined γ' phase alloy can be expected not to be significantly changed.

TMS-238 has excellent microstructural stability among the advanced generation superalloys containing Rhenium. In this study, RPR method keeps approximately 30 min at the target temperatures during the resonance frequency measurement, but this holding period is significantly short for TCP precipitation in TMS-238 as reported in previous study because TMS-238 does not contain TCP phase around 200 h aging at 900, 1000, and 1100 °C [53]. TCP phase is expected to nucleate from γ matrix channel [54] which is equilibrium with γ' phase [55]. Furthermore, based on the above microstructural observation, pronounced TCP phase affecting elastic modulus is not expected in the tie-lined γ' phase alloy because of small fraction of γ phase. In the case of the tie-lined γ phase alloy, TCP phase precipitation is not expected because no γ' phase is expected above 900 °C. Additionally, the effect of solidification segregation on the measured elastic modulus is minor. This is because the measured elastic modulus is obtained from specimens that contain both dendritic and inter-dendritic regions. Given the compositional differences between these regions, each has a distinct elastic modulus. However, since the specimen as a whole can be regarded as a composite material comprising dendritic and inter-dendritic regions, the measured

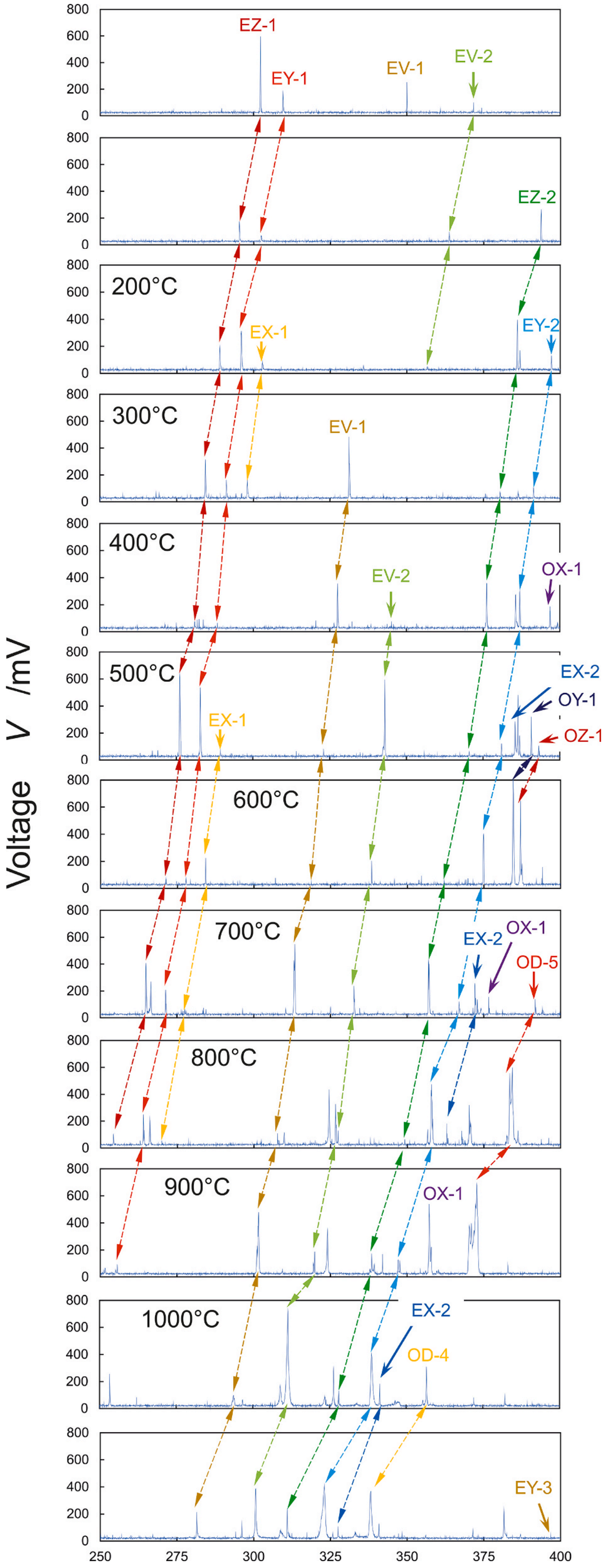

Fig. 3. Experimental resonance frequency of TMS-238 between 250 and 400 kHz, and its temperature dependence in each resonance mode.

elastic modulus represents an averaged value between them.

3.2. *Rectangular parallelepiped resonance method*

Fig. 3 shows an example in obtained frequency spectra of the TMS-238 between room temperature and 1100 °C in the range from 250 to 400 kHz although actual experiments were conducted in the range between 250 and 1250 kHz. Frequency of each peak consisting of the spectra decreased with the increase of temperature. Therefore, to confirm validity of the analysis, the analysis to fit experimental spectra was conducted to show continuous decrease of each simulated resonance frequency with the increase of temperature, as shown in Fig. 4, which shows an example in the resonance frequency with EV-mode. This validation was conducted to all resonance mode of OD, EV, OX, OY, OZ, EX, EY and EZ, from 1st to 8th resonance frequency.

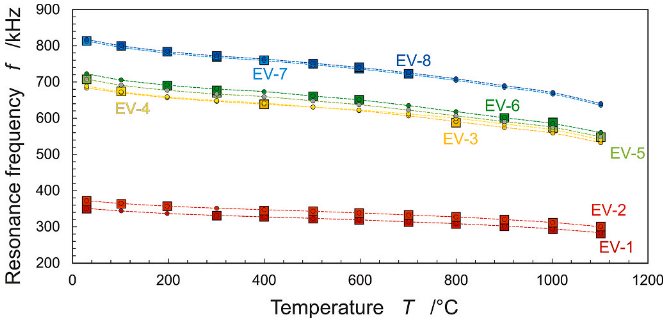

Fig. 4. Temperature dependence of resonance frequency with EV-mode in TMS-238. Square plots indicate expreimtnal resoncne frequencies, and round plots indicate simulated ones. Dashed lines indicates connection between simulated resonance frequencies with the same mode in different temperatures.

3.3. *Elastic modulus of TMS-238 and its tie-lined γ and γ' phase alloys*

Using RPR method, elastic constants of c_{11}, c_{12}, and c_{44} were obtained. Furthermore, typically used elastic moduli were calculated using c_{11}, c_{12}, and c_{44}. This research mainly focuses on a longitudinal elastic modulus along <100> defined by equation (2), which is a component of the elastic misfit for alloy design [34,35]. The experimental <100> longitudinal elastic modulus are shown in Fig. 5 as plots. Furthermore, shear modulus c' on {110} to <110> defined by equation (3) is also calculated, and shown in Fig. 5. Detailed elastic moduli of TMS-238 and its tie-lined alloys are shown in Table A1 in Appendix A. This is because the longitudinal elastic modulus E, shear modulus c_{44}, and c' have a high accuracy by RPR method because the resonance spectra of specimens are sensitive to those elastic moduli [38,56].

$$E = \frac{(c_{11} - c_{12})(c_{11} + 2c_{12})}{c_{11} + c_{12}} \tag{2}$$

$$c' = \frac{c_{11} - c_{12}}{2} \tag{3}$$

For the convenience for many researchers, temperature dependence of the elastic modulus with high accuracy in RPR method was derived using regression approach by equation (4) for longitudinal elastic modulus as well as other two shear moduli with high accuracy. Elastic modulus M is explained by equation (4).

$$M = D_0 + T \cdot D_T + T^2 \cdot D_{T^2} + T^3 \cdot D_{T^3} \tag{4}$$

c_{11} and c_{12} can be deduced using predicted values of longitudinal elastic modulus E, and shear moduli c', as following equations.

$$c_{11} = \frac{-E \cdot c' + 4 \cdot c'^2}{3c' - E} \tag{5}$$

$$c_{12} = \frac{E \cdot c' - 2 \cdot c'^2}{3c' - E} \tag{6}$$

The predicted values of elastic modulus, E, c_{44}, and c' are shown in Fig. 5 as lines, and the coefficient of determination in the equations for each tie-lined alloy are over 0.99. Each regression coefficient for each

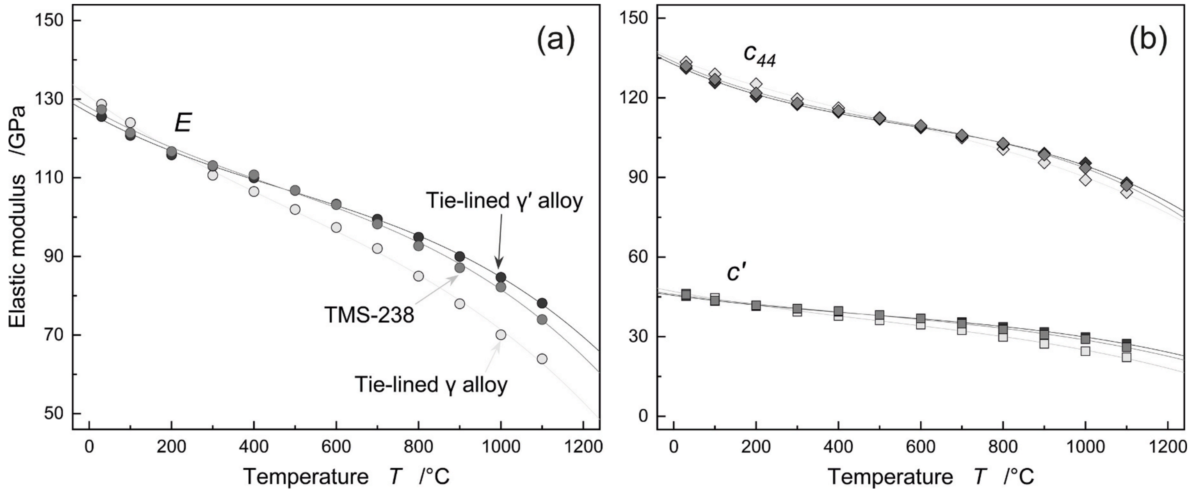

Fig. 5. Temperature dependence of the elastic modulus of TMS-238 and its tie-lined alloys.
(a) <100> longitudinal elastic modulus, (b) shear modulus Plots indicate experimental elastic modulus, and lines indicate predicted elastic modulus using equation (4).

Table 3
Regression coefficients for elastic moduli for TMS-238 and its tie-lined alloys.

M	Terms	D_0	D_T	D_{T^2}	D_{T^3}
	Unit	/GPa	/GPa·K^{-1}	/GPa·K^{-2}	/GPa·K^{-3}
E	TMS-238	1.487×10^{2}	-9.602×10^{-2}	-8.230×10^{-5}	-3.796×10^{-8}
	Tie-lined γ phase alloy	1.560×10^{2}	-1.129×10^{-1}	-8.316×10^{-5}	-3.667×10^{-8}
	Tie-lined γ′ phase alloy	1.469×10^{2}	-9.466×10^{-2}	-8.303×10^{-5}	-3.695×10^{-8}
c_{44}	TMS-238	1.603×10^{2}	-1.272×10^{-1}	1.223×10^{-4}	-4.999×10^{-8}
	Tie-lined γ phase alloy	1.548×10^{2}	-8.863×10^{-2}	6.547×10^{-5}	-2.813×10^{-8}
	Tie-lined γ′ phase alloy	1.590×10^{2}	-1.258×10^{-1}	1.203×10^{-4}	-4.818×10^{-8}
c'	TMS-238	5.311×10^{1}	-3.256×10^{-2}	2.624×10^{-5}	-1.234×10^{-8}
	Tie-lined γ phase alloy	5.694×10^{1}	-4.437×10^{-2}	3.338×10^{-5}	-1.436×10^{-8}
	Tie-lined γ′ phase alloy	5.309×10^{1}	-3.487×10^{-2}	3.033×10^{-5}	-1.358×10^{-8}

alloy is shown in Table 3.

4. Discussion

Based on microstructural observation, this article focuses on the determination of elastic modulus using tie-lined alloys above 900 °C, where cooling γ′ precipitates in γ phase alloy are not expected.

4.1. *Composite model for cubic γ′ precipitates*

As shown in Fig. 2(g), 2(h), and 2(i), the tie-lined γ′ phase alloy is expected to have γ phase at 900 °C. Therefore, the elastic modulus of pure γ′ phase should be simulated by other method using the elastic modulus of the tie-lined alloys. To solve this problem, composite models of the elastic modulus were used to estimate the elastic modulus of pure γ′ phase in the tie-lined alloys by using the elastic modulus of the tie-lined γ phase alloy and TMS-238.

As the composite models, traditional composite models called Voigt [57] and Reuss [58] rules in addition to a newly established one called Model A were used. Since Voigt and Reuss rules can predict upper and lower limits of the elastic modulus in composite microstructure, these rules can simulate the range of simulated elastic modulus of pure γ′ phase. Furthermore, Model A simulates the elastic modulus based on realistic microstructure of superalloys. This is because Model A was established by assuming the microstructure in TMS-238 with aligned and cubic γ′ precipitates, however, Voigt and Reuss models assume raft-like precipitates, which is not identical to original microstructure of TMS-238 as shown in Fig. 2. Equation (7) and equation (8) are equations for <100> longitudinal elastic modulus in composite microstructure deduced by Voigt and Reuss models, respectively. Equation (9) is <100> longitudinal elastic modulus in composite microstructure specialized for conventional Ni-base single-crystal superalloys deduced by Model A. γ′ volume fraction $V_{\gamma'}$ shown in equation (10) is calculated by dimension ratio in microstructure only in Model A, which is detailly introduced in Fig. 7, where a is edge length of cubic γ′ precipitates, and b is edge length of a unit cell. Notably, there is no restraint condition between γ′ volume fraction and dimension ratio in Voigt and Reuss models. Model A can apply for other elastic moduli such as c_{44} and c' as in the same case of other mixture models, such as Voigt and Reuss models [37]. Notably, these composite models do not contain inhomogeneous effect by solidification segregation, therefore, output of the elastic modulus by these composite models is average values of specimens.

$$E_{Voigt} = E_{\gamma} \cdot \left(1 - V_{\gamma'}\right) + E_{\gamma'} \cdot V_{\gamma'} \tag{7}$$

$$E_{Reuss} = \frac{E_{\gamma} \cdot E_{\gamma'}}{E_{\gamma} \cdot V_{\gamma'} + E_{\gamma'}\left(1 - V_{\gamma'}\right)} \tag{8}$$

$$E_A = \frac{\left(\left(1 - x^2\right) \cdot E_{\gamma} + x^2 \cdot E_{\gamma'}\right) \cdot E_{\gamma}}{(1 - x) \cdot \left(\left(1 - x^2\right) \cdot E_{\gamma} + x^2 \cdot E_{\gamma'}\right) + x \cdot E_{\gamma}} \tag{9}$$

$$V_{\gamma'} = \left(\frac{a}{b}\right)^3 = x^3 \tag{10}$$

Fig. 6 shows assumptions to establish Model A which has a unit cell of conventional Ni-base single-crystal superalloy with aligned and cubic

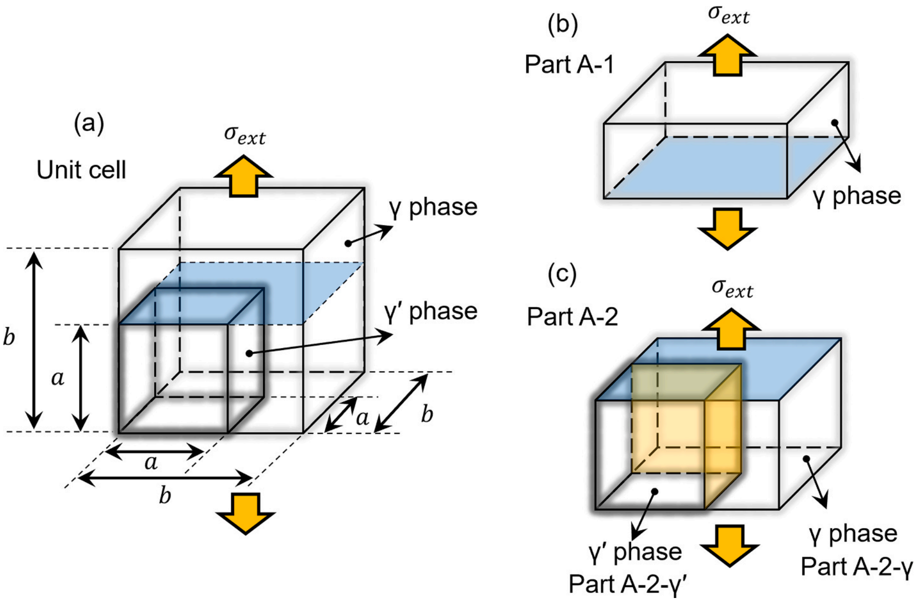

Fig. 6. Assumption to establish Model A in a unit cell.
(a) Assembled parts using Fig. 6 (b) and 6 (c), (b) divided part called Part A-1 consisting of γ matrix, and (c) divided part called Part A-2 consisting of γ matrix called Part A-2-γ and of γ′ precipitate called Part A-2-γ′

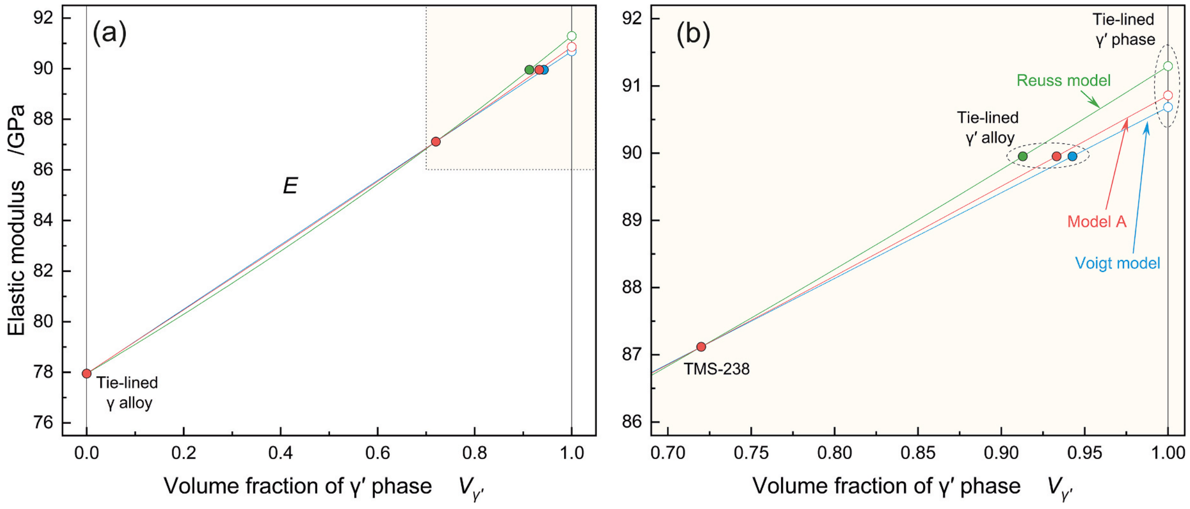

Fig. 7. <100> longitudinal elastic modulus of TMS-238 and its tie-lined phase alloys at 900 °C
(a) volume fraction dependency of γ′ phase on the elastic modulus, (b) side in γ′ phase.

γ′ precipitates. Model A in Fig. 6 (a) consists of two parts called Part A-1 and Part A-2 shown in Fig. 6 (b) and 6 (c), respectively. Model A assumes that the same external applied stress σ_{ext} is applied to Part A-1 and Part A-2. However, the external applied stress is redistributed to each part of Part A-2, Part A-2-γ′ and Part A-2-γ in Fig. 6 (c) to keep unit cell, mainly from the reason of the difference in the elastic modulus between γ and γ′ phase. Detailed procedure to deduce Model A is described in Appendix B.

4.2. Determination of tie-lined elastic modulus by new model at 900 °C

To obtain elastic modulus of the pure γ′ phase at 900 °C, the elastic moduli of tie-lined γ phase alloy and TMS-238 with their volume fraction of γ′ phase were input into all the composite models, Reuss, Voigt, and Model A. Output of the elastic moduli of γ′ phase by Reuss and Voigt models offers upper and lower boundaries of elastic modulus of pure γ′ phase respectively, and Model A is expected to show the elastic modulus of pure γ′ phase based on realistic microstructure if volume fraction of γ′ phase is set as 1. The results of the estimation by each model is shown in Fig. 7. This approach tells us that the <100> longitudinal elastic modulus of pure γ′ phase at 900 °C by Model A is expected to be 90.86 GPa (Maximum: 91.29 GPa, Minimum: 90.68 GPa). Also, γ′ volume fraction of tie-lined γ′ phase alloy is calculated to be 0.93 (Maximum: 0.95, Minimum: 0.90).

4.3. Determination of the elastic modulus of the pseudo-tie-lined phases at 1000 and 1100 °C

Fig. 8 shows temperature dependence of equilibrium compositions in the individual γ and γ′ phases and TMS-238, based on Table 1 calculated by ADP, for some characteristic γ former elements Co and Re, and γ′ former elements Al and Ta. Fig. 8 (a) shows that equilibrium compositions of Al in γ phase increases as temperature increases, however, those in γ′ phase show almost constant values. In addition, equilibrium

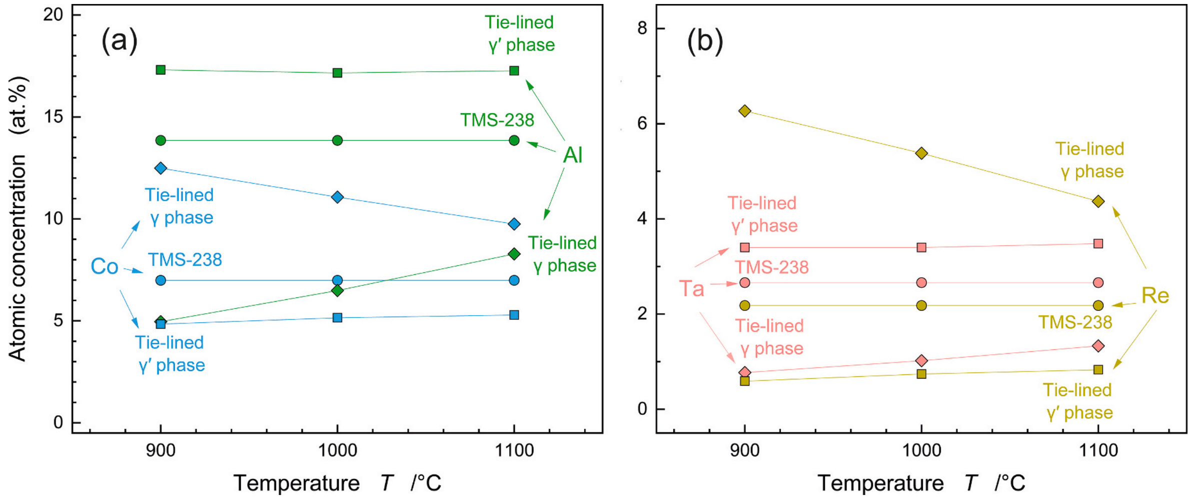

Fig. 8. Equilibrium compositions of γ and γ′ phases and TMS-238 by ADP.
(a) Main elements Co for γ former and Al for γ′ former, (b) heavy elements Re for γ former and Ta for γ′ former.

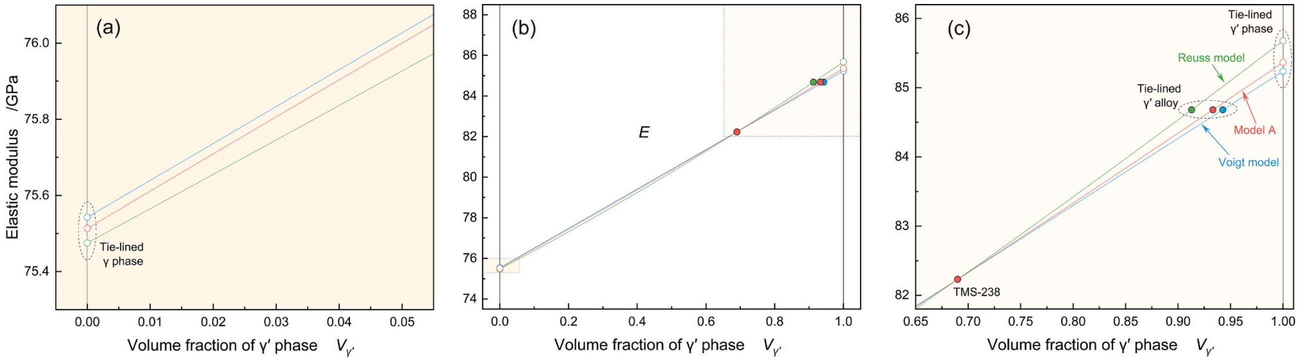

Fig. 9. Elastic modulus of a series of the tie-lined TMS-238 alloys at 1000 °C
(a) Side in γ phase, (b) volume fraction dependency of γ′ phase on the elastic modulus, and (c) side in γ′ phase.

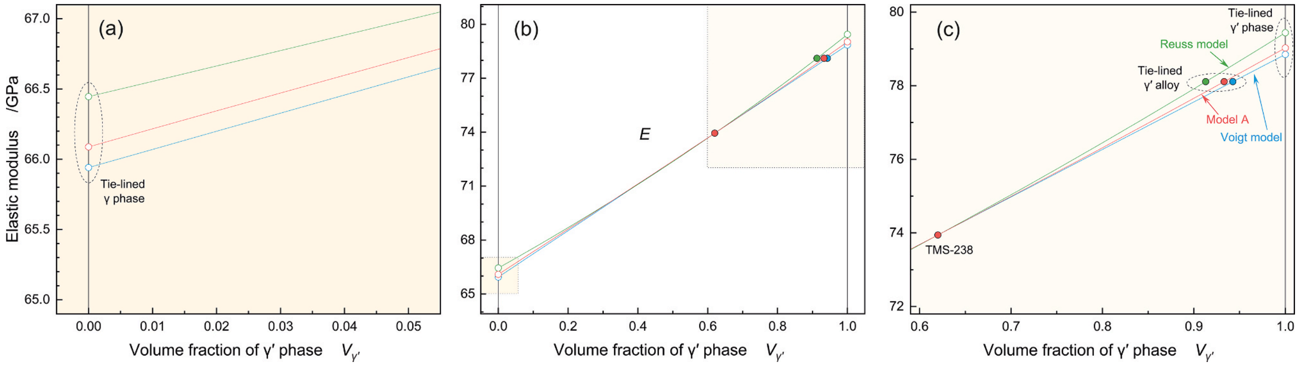

Fig. 10. Elastic modulus of a series of the tie-lined TMS-238 alloys at 1100 °C
(a) Side in γ phase, (b) volume fraction dependency of γ′ phase on the elastic modulus, and (c) side in γ′ phase.

concentration of Co in γ phase decreases as temperature increases, however, that in γ′ phase shows almost constant value. Now, we have to remember again that tie-lined alloys based on TMS-238 have been designed so as to be in equilibrium at 900 °C. Larger change in equilibrium compositions in γ phase with temperatures indicates that the elastic modulus of tie-lined γ phase alloy over 900 °C, such as 1000 and 1100 °C, is differ from exact elastic modulus of equilibrium situation at these temperatures, and needs to be estimated by some approaches. On the other hand, almost constant equilibrium compositions in γ′ phase with temperatures indicate that the elastic modulus of tie-lined γ′ phase alloy over 900 °C could be close to that of pure γ′ phase determined by the same approach to estimate the elastic modulus used in previous section at 900 °C.

This section focuses on the determination of the elastic modulus at 1000 and 1100 °C. Based on the above consideration, the elastic modulus of equilibrium γ and γ′ phases at these temperatures needs to be determined using the elastic modulus of TMS-238 and tie-lined γ′ phase alloy, using each composite model. Since the equilibrium compositions

Table 4
Elastic modulus of TMS-238 and its tie-lined phases at elevated temperatures.

	T /°C	E /GPa	c_{11} /GPa	c_{12} /GPa	c_{44} /GPa	c' /GPa	ν –	B /GPa	A –
TMS-238	900	87.12	217.80	156.36	98.55	30.72	0.4179	176.84	3.208
	1000	82.23	205.06	147.05	93.58	29.00	0.4176	166.39	3.227
	1100	73.94	192.42	140.42	86.96	26.00	0.4219	157.75	3.344
Tie-lined γ phase	900	77.95	219.26	164.71	95.60	27.27	0.4290	182.89	3.505
	1000	75.51	177.58	124.07	85.90	26.75	0.4113	141.90	3.211
	1100	66.09	159.31	112.57	84.36	23.37	0.4141	128.15	3.610
Tie-lined γ′ phase	900	90.86	218.60	154.33	99.71	32.13	0.4138	175.75	3.103
	1000	85.36	218.71	158.61	97.17	30.05	0.4204	178.64	3.233
	1100	79.03	215.86	160.46	88.58	27.70	0.4264	178.93	3.198

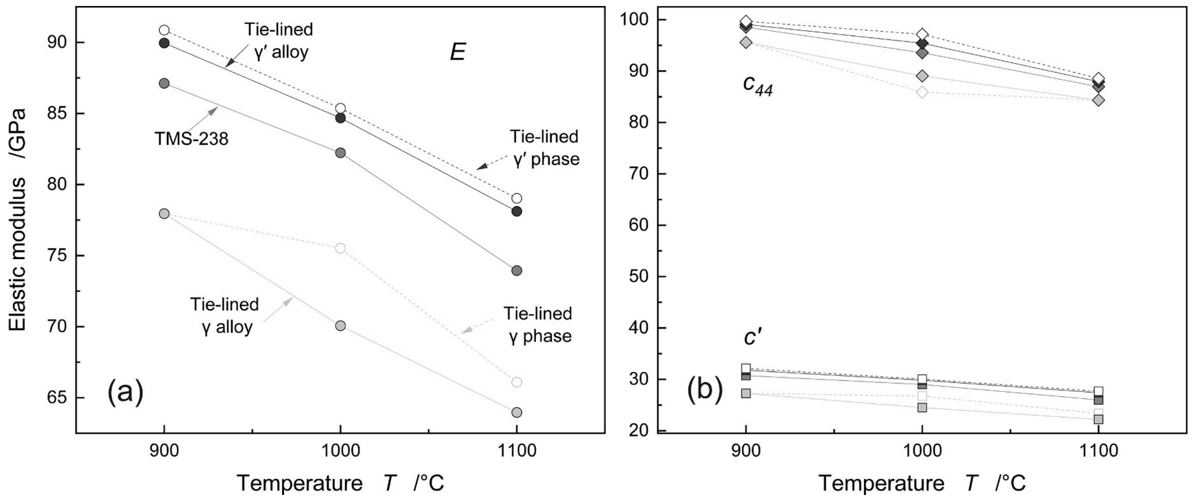

Fig. 11. Temperature dependence of the elastic modulus of TMS-238 and its tie-lined phases at elevated temperatures.
(a) <100> longitudinal elastic modulus, (b) shear modulus.

of γ′ phase is almost constant regardless temperatures, and since nominal compositions of tie-lined γ′ phase alloy is close to phase boundary of γ′ phase, volume fraction of γ phase in tie-lined γ′ phase alloy at 1000 and 1100 °C is assumed to be the same values at 900 °C, determined by each composite model. Using this approach, the elastic moduli of equilibrium γ and γ′ phases at 1000 °C was estimated as shown in Fig. 9, and those at 1100 °C was also estimated as shown in Fig. 10. The elastic modulus of γ phase was estimated as 75.51 GPa (Maximum: 75.54 GPa, Minimum: 75.48 GPa) at 1100 °C, and as 66.01 GPa (Maximum: 65.94 GPa, Minimum: 66.45 GPa) at 1100 °C, and that of γ′ phase was estimated as 85.36 GPa (Maximum: 85.68 GPa, Minimum: 85.24 GPa), and as 79.03 GPa (Maximum: 79.44 GPa, Minimum: 78.85 GPa).

4.4. Comparison of the elastic modulus of TMS-238 with other alloy systems

Other elastic modulus of shear modulus such as c_{44} and c' were also obtained at 900, 1000, and 1100 °C in the same manner of longitudinal elastic modulus E using composite model of Model A. Using values of c' and E, c_{11} and c_{12} were also obtained, then other important elastic moduli can be also calculated such as Poisson's ratio $\nu = \frac{c_{12}}{c_{11}+c_{12}}$, bulk modulus $B = \frac{c_{11}+2c_{12}}{3}$, anisotropic factor $A = \frac{2c_{44}}{c_{11}-c_{12}}$. Table 4 lists these elastic moduli of the tie-lined TMS-238 at higher temperatures, and Fig. 11 shows the comparison of their elastic modulus as a figure, focusing on elastic modulus with high reliability such as longitudinal elastic modulus and shear modulus. According to Fig. 11, the elastic modulus of the tie-lined γ′ phase is close to those of tie-lined γ′ phase alloy, indicating that remained γ matrix has small effect on the elastic modulus. For instance, the difference of the longitudinal elastic modulus between tie-lined γ′ phase alloy and estimated tie-lined γ′ phase is below 1 GPa at each temperature. However, larger deviation of the elastic modulus of the tie-lined γ phase from that of tie-lined γ phase alloy was confirmed, indicating that deviation of constituting elements from those at 900 °C is significant for the elastic modulus. For instance, the deviation of the longitudinal elastic modulus at 1000 °C is 5.5 GPa, and that at 1100 °C is 2.1 GPa.

Effect of the alloying elements on the elastic modulus is significant for the alloy design. To compare the elastic modulus of tie-lined phases in TMS-238, the elastic modulus of tie-lined phases in Ni-Al systems was also estimated. According to published phase diagram of Ni-Al system [52], equilibrium compositions of Al in γ-γ′ two-phases region are summarized in Table 5.

To estimate the elastic modulus of the compositions shown in Table 5 predictive equations of the elastic modulus M for Ni-Al systems were established though regression approach with equation (11) where c_{Al} is

Table 5
Equilibrium Al concentrations in the region of γ-γ′ two phase systems in Ni-Al from phase diagram [52].

	Tie-lined γ phase			Tie-lined γ′ phase		
Temperature/°C	900	1000	1100	900	1000	1100
Al (at.%)	14.69	15.64	17.07	23.17	22.69	22.94

Table 6
Regression coefficients for elastic modulus of the individual γ and γ′ phases in Ni-Al system.

M	Phases	D_0 / GPa	D_T / $GPa \cdot K^{-1}$	D_{T^2} / $GPa \cdot K^{-2}$	D_{T^3} / $GPa \cdot K^{-3}$	$D_{c_{Al}}$ / GPa
E	γ	1.479×10^2	-1.210×10^{-1}	1.123×10^{-4}	-4.888×10^{-8}	-4.504×10^{-1}
	γ′	1.318×10^2	-1.1140×10^{-1}	1.250×10^{-4}	-5.614×10^{-8}	-1.005
c_{44}	γ	1.491×10^2	-1.290×10^{-1}	1.271×10^{-4}	-5.075×10^{-8}	-1.751×10^{-1}
	γ′	1.469×10^2	-9.970×10^{-2}	1.056×10^{-4}	-4.855×10^{-8}	-3.448×10^{-1}
c'	γ	5.313×10^1	-4.161×10^{-2}	3.657×10^{-5}	-1.595×10^{-8}	-1.715×10^{-1}
	γ′	4.748×10^1	-4.230×10^{-2}	4.640×10^{-5}	-2.075×10^{-8}	-4.430×10^{-1}

atomic concentration of Al, using referenced data of Pure Ni [35], Ni-12.69 Al [59], and Ni-14.69 Al [35] for γ single phase, and data of Ni-23.17Al [35], Ni-23.20Al [60], Ni-24.0Al [60], and Ni-25.0Al [60] for γ′ single phase. All the referenced elastic moduli were obtained using RPR method, which is the same method in this research. Notably, to escape from the effect of cooling γ′ phase in γ single phase alloys on the elastic modulus, referenced data in the γ-γ′ two-phase region was omitted based on published Ni-Al phase diagram [52]. Obtained regression coefficients in equation (11) are listed in Table 6, and detailed elastic moduli of Pure Ni, Ni-14.69Al, and Ni-23.17Al measured by authors using RPR method are shown in Table A2 in Appendix A.

$$M = D_0 + T \cdot D_T + T^2 \cdot D_{T^2} + T^3 \cdot D_{T^3} + c_{Al} \cdot D_{c_{Al}} \tag{11}$$

Fig. 12 shows the elastic modulus of tie-lined γ phase in PureNi, Ni-Al system, and TMS-238. In Fig. 12, longitudinal elastic modulus and shear modulus of tie-lined γ phase in PureNi are close to those in TMS-238, but those of Ni-Al system are lower than those in PureNi and TMS-238.

Fig. 13 also shows the elastic modulus of equilibrium γ′ phase in Ni-Al system and TMS-238. In the similar manner to the case of the elastic modulus of γ phase, longitudinal elastic modulus and shear modulus of

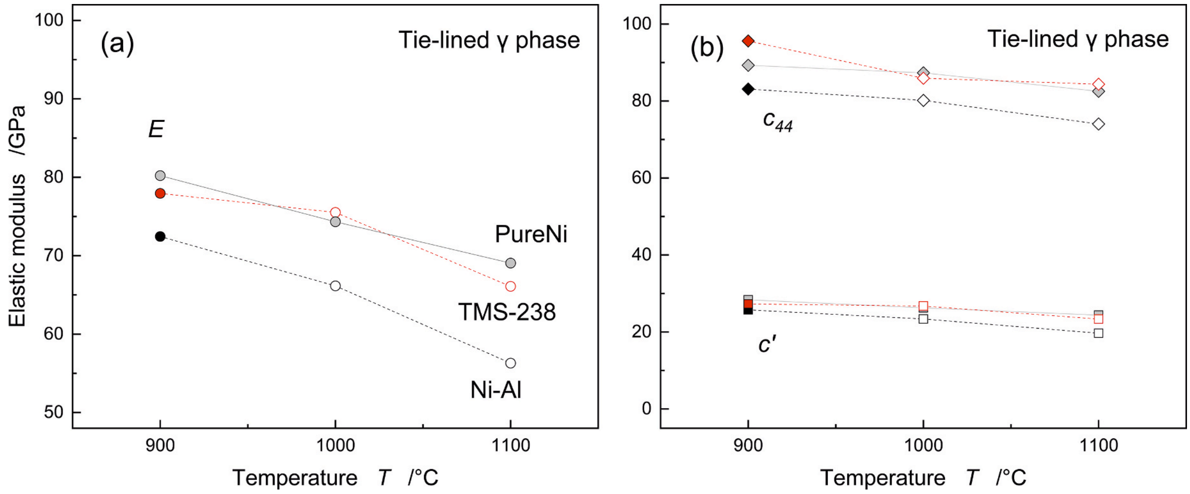

Fig. 12. Comparison of elastic modulus in tie-lined γ phase in alloys with γ and γ′ phases.
(a) longitudinal elastic modulus, (b) shear modulus. Closed plots show experimental data, and open plots show predicted data.

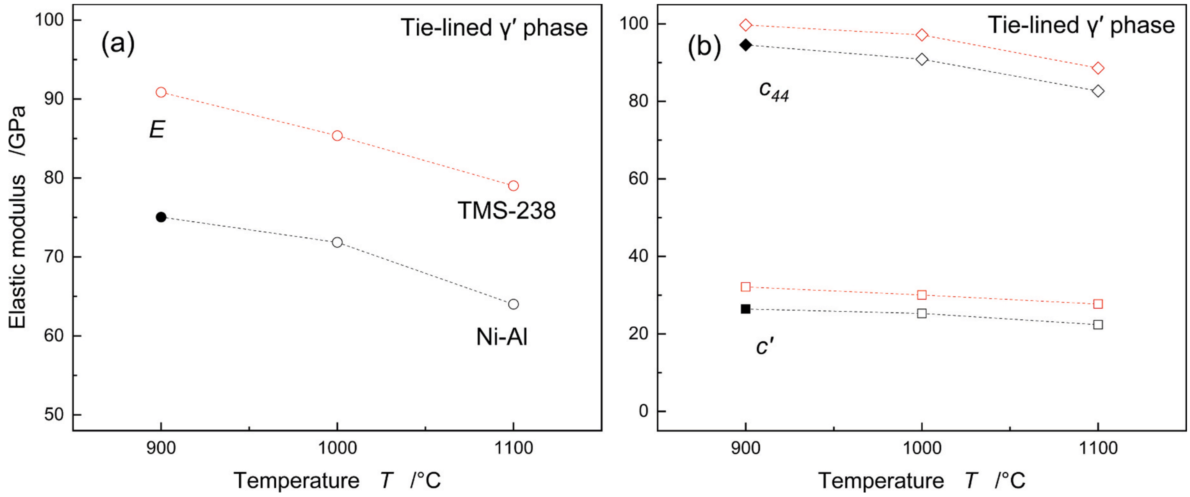

Fig. 13. Comparison of elastic modulus in tie-lined γ′ phase in alloys with γ and γ′ phases.
(a) longitudinal elastic modulus, (b) shear modulus. Closed plots show experimental data, and open plots show predicted data.

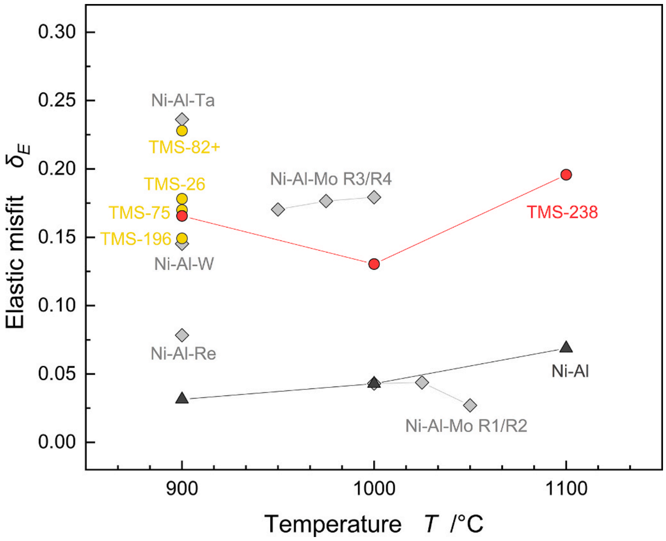

Fig. 14. Comparison of the elastic misfit by tie-lined γ and γ' phases at elevated temperatures.
Data of conventional alloys such as TMS-26 [35], TMS-82+[35], TMS-75 [35], and TMS-196 [35], Ni-Al-X tertiary alloys such as Ni-Al-Ta [35], Ni-Al-W [35], Ni-Al-Re [35], and Ni-Al-Mo [37] are calculated from references. Data of Ni-Al system and TMS-238 comes from this research.

equilibrium γ' phase in Ni-Al system are lower than those in TMS-238.

Comparing the elastic modulus of TMS-238 with conventional alloys is also significant for practical use, therefore, Appendix C summarizes the elastic modulus of several conventional alloys with that of TMS-238.

Fig. 14 summarizes the elastic misfit of defined by $\delta_E = \frac{E_{\gamma'} - E_{\gamma}}{E_{\gamma}}$ in Ni-Al binary system, Ni-Al-X tertiary systems, TMS-238 and other conventional superalloys. All the elastic misfit among investigated alloys is positive. Fig. 14 also shows that the elastic misfit differs from alloys, implying its compositional dependence [33]. The elastic misfit of TMS-238 is almost equivalent to those of other conventional alloys such as TMS-26, TMS-75, and TMS-196, furthermore, Ni-Al-W and Ni-Al-Mo R3/R4 tertiary systems. The elastic misfit of TMS-82+ and Ni-Al-Ta are larger than those of TMS-238. However, the elastic misfit of Ni-Al binary system, Ni-Al-Re, and Ni-Al-Mo R1/R2 tertiary systems are smaller than those of TMS-238. Notably, in the reference of Ni-Al-Mo system [37], R1 and R3 are alloys with γ and γ' phases but each alloy has different compositions. R2 is the tie-lined γ single phase alloy equilibrium with R1, and R4 is another tie-lined γ single phase alloy equilibrium with R3. Therefore, the elastic misfit in equilibrium γ and γ' phases in Ni-Al-Mo system can be calculated from the data set of R1/R2 and that of R3/R4, respectively.

5. Conclusion

This manuscript reports the elastic moduli of 6th generation Ni-base single crystal superalloy TMS-238 and its tie-lined γ and γ' phases , using newly developed composite model.

1. Tie-lined TMS-238 alloys which are equilibrium at 900 °C were designed and fabricated. Microstructural observation revealed that γ' single phase alloy contains small amount of γ phase especially distributed in dendrite-core region although γ single phase alloy contains homogeneously distributed fine γ' precipitates, expecting dissolution above 900 °C.
2. Elastic modulus of TMS-238 and its tie-lined alloys were measured using RPR method from room temperature to 1100 °C. Furthermore, the elastic moduli of equilibrium phases were determined above 900 °C using newly developed composite models.
3. Elastic moduli of equilibrium γ phase in TMS-238 are almost equivalent to those of PureNi, but they are larger than those in Ni-Al system. In the same way, the elastic moduli of equilibrium γ' phase in TMS-238 are larger than those in Ni-Al system.
4. Elastic misfit, defined by $\delta_E = \frac{E_{\gamma'} - E_{\gamma}}{E_{\gamma}}$ which is an important factor for raft structure formation, in TMS-238 was evaluated and compared with other alloy systems. The elastic misfit among all the investigated alloys is positive. The elastic misfit of TMS-238 is intermediate value, among all the investigated alloy systems. This implied that the alloy compositions changes the elastic misfit.

CRediT authorship contribution statement

Takuma Saito: Writing – review & editing, Writing – original draft, Visualization, Validation, Methodology, Investigation, Formal analysis, Data curation, Conceptualization. **Hiroshi Harada:** Writing – review & editing, Supervision, Resources, Conceptualization. **Makoto Osawa:** Writing – review & editing, Validation, Methodology. **Tadaharu Yokokawa:** Validation, Software, Methodology. **Kyoko Kawagishi:** Writing – review & editing, Resources. **Shinsuke Suzuki:** Writing – review & editing, Resources.

Declaration of competing interest

The authors declare that they have no known competing financial interests or personal relationships that could have appeared to influence the work reported in this paper.

Acknowledgement

This work was supported by Japan Science and Technology Agency (JST) under the Advanced Low Carbon Technology Research and Development Program (ALCA) project “Development of Direct and Complete Recycling Method for Superalloy Turbine Aerofoils.” JST ALCA Grant Number JPMJAL1302, Japan. In addition, this work is partially suppoted by the New Energy and Industrial Technology Development Organization (NEDO) under the the project "Aero Engine Materials Development and Evaluation Sysstem Infratructure Development Project." NEDO Grant Number JPNP21007.

Appendix A. Detailed elastic modulus measured using RPR method

Table A1 summarizes detailed elastic moduli of TMS-238 and its tie-lined γ and γ' phase alloys. E, c', and c_{44} of these alloys are shown in Fig. 5, as plots. Furthermore, Table A2 also summarizes detailed elastic moduli of PureNi, Ni-14.69Al, and Ni-23.17Al, which were used to deduce the regression coefficients of elastic modulus in Ni-Al system, shown in Table 6. Longitudinal elastic modulus E of these alloys measured by the authors are shown in previous works as plots in figures [33].

Table A1
Elastic moduli of TMS-238 and its tie-lined γ and γ′ phase alloys, measured using RPR method.

Specimen	T	E	c_{11}	c_{12}	c_{44}	c'	ν	B	A
	/°C	/GPa	/GPa	/GPa	/GPa	/GPa	–	/GPa	–
TMS-238	30	127.35	253.24	161.59	131.97	45.825	0.3895	192.14	2.880
	100	121.43	249.64	162.56	126.97	43.542	0.3944	191.58	2.916
	200	116.67	240.36	156.71	121.79	41.829	0.3947	184.59	2.912
	300	113.11	233.68	152.61	118.01	40.538	0.3951	179.63	2.911
	400	110.73	227.33	147.90	115.14	39.713	0.3942	174.38	2.899
	500	106.81	228.76	152.47	112.36	38.149	0.3999	177.90	2.945
	600	103.17	220.51	146.80	109.53	36.856	0.3997	171.37	2.972
	700	98.26	223.29	153.48	105.92	34.908	0.4073	176.75	3.034
	800	92.69	227.67	162.21	102.83	32.728	0.4161	184.03	3.142
	900	87.12	217.80	156.36	98.55	30.721	0.4179	176.84	3.208
	1000	82.23	205.06	147.05	93.58	29.003	0.4176	166.39	3.227
	1100	73.94	192.42	140.42	86.96	26.003	0.4219	157.75	3.344
Tie-lined γ′ phase alloy	30	128.68	260.20	167.76	133.44	46.220	0.3920	198.57	2.887
	100	124.00	248.15	158.97	128.96	44.591	0.3905	188.70	2.892
	200	116.57	257.13	174.08	125.25	41.523	0.4037	201.76	3.017
	300	110.65	246.97	168.23	119.58	39.372	0.4052	194.48	3.037
	400	106.50	244.35	168.74	116.21	37.806	0.4085	193.95	3.074
	500	101.93	236.59	164.29	112.54	36.152	0.4098	188.39	3.113
	600	97.35	225.12	156.05	108.76	34.538	0.4094	179.07	3.149
	700	92.00	229.40	164.50	104.94	32.447	0.4176	186.13	3.234
	800	84.98	219.46	159.66	100.61	29.900	0.4211	179.59	3.365
	900	77.95	219.26	164.71	95.60	27.275	0.4290	182.89	3.505
	1000	70.06	198.25	149.24	89.06	24.506	0.4295	165.57	3.634
	1100	63.96	208.42	164.02	84.34	22.202	0.4404	178.82	3.799
Tie-lined γ′ phase alloy	30	125.56	246.80	156.33	131.16	45.237	0.3878	186.48	2.900
	100	120.77	243.15	156.35	125.74	43.400	0.3914	185.28	2.897
	200	115.82	237.18	154.08	120.59	41.549	0.3938	181.78	2.902
	300	112.93	231.32	150.30	117.51	40.511	0.3939	177.30	2.901
	400	109.97	227.73	148.93	114.67	39.404	0.3953	175.20	2.910
	500	106.77	228.31	152.03	111.97	38.141	0.3997	177.46	2.936
	600	103.27	221.75	148.00	108.90	36.876	0.4003	172.58	2.953
	700	99.47	216.67	145.72	105.48	35.473	0.4021	169.37	2.973
	800	94.89	219.88	152.56	102.48	33.659	0.4096	175.00	3.045
	900	89.95	218.05	154.46	99.09	31.794	0.4147	175.66	3.117
	1000	84.68	215.44	155.79	95.42	29.824	0.4197	175.67	3.199
	1100	78.11	211.13	156.33	87.94	27.399	0.4254	174.60	3.210

Table A2
Elastic moduli of PureNi, Ni-14.69Al, and Ni-23.17Al, measured using RPR method.

Specimen	T	E	c_{11}	c_{12}	c_{44}	c'	ν	B	A
	/°C	/GPa	/GPa	/GPa	/GPa	/GPa	–	/GPa	–
PureNi	30	120.11	230.04	143.24	120.14	43.40	0.38373	172.17	2.768
	400	103.06	206.88	132.78	105.00	37.05	0.39092	157.48	2.834
	500	99.07	200.85	129.70	101.99	35.57	0.39238	153.42	2.867
	600	95.28	201.28	133.13	98.22	34.07	0.39811	155.85	2.883
	700	90.45	204.52	140.22	95.69	32.15	0.40674	161.65	2.976
	800	86.32	191.49	130.02	92.77	30.73	0.40441	150.51	3.019
	900	80.20	191.61	134.85	89.27	28.38	0.41307	153.77	3.146
	1000	74.33	178.81	126.23	87.33	26.29	0.41382	143.76	3.322
	1100	69.06	169.88	121.11	82.53	24.38	0.41621	137.37	3.385
Ni-14.69Al	30	111.16	216.70	136.53	110.95	40.09	0.38652	163.25	2.768
	100	107.79	210.31	132.58	107.92	38.87	0.38665	158.49	2.777
	200	102.24	197.92	124.13	103.77	36.90	0.38543	148.73	2.813
	300	96.98	191.02	121.15	99.08	34.93	0.38810	144.44	2.836
	400	93.20	178.93	111.59	96.69	33.67	0.38411	134.04	2.872
	500	88.79	174.98	111.01	94.31	31.98	0.38817	132.33	2.949
	600	84.90	170.76	109.74	92.43	30.51	0.39122	130.08	3.029
	700	80.97	163.71	105.54	90.49	29.09	0.39198	124.93	3.111
	800	77.42	161.40	105.96	87.71	27.72	0.39630	124.44	3.164
	900	72.45	162.64	111.11	83.13	25.77	0.40588	128.29	3.227
	1000	66.15	160.53	113.78	80.17	23.38	0.41478	129.36	3.429
	1100	56.30	159.00	119.61	74.03	19.69	0.42931	132.74	3.759
Ni-23.17Al	30	105.21	231.06	156.08	123.84	37.49	0.40316	181.07	3.303
	100	102.02	228.49	155.91	122.17	36.29	0.40559	180.11	3.366
	200	96.82	222.88	154.15	116.68	34.36	0.40887	177.06	3.396
	300	92.43	217.73	152.25	112.38	32.74	0.41150	174.08	3.432

(*continued on next page*)

Table A2 (*continued*)

Specimen	T /°C	E /GPa	c_{11} /GPa	c_{12} /GPa	c_{44} /GPa	c' /GPa	ν –	B /GPa	A –
	400	89.43	210.94	147.59	109.51	31.68	0.41165	168.71	3.457
	500	86.47	208.51	147.36	106.76	30.58	0.41408	167.74	3.492
	600	83.81	203.23	143.98	104.21	29.62	0.41469	163.73	3.518
	700	81.05	198.15	140.90	101.77	28.63	0.41556	159.98	3.555
	800	77.98	194.67	139.67	98.13	27.50	0.41775	158.01	3.568
	900	75.04	190.74	137.88	94.59	26.43	0.41957	155.50	3.579
	1000	71.85	185.77	135.22	90.87	25.28	0.42125	152.07	3.595
	1100	64.01	180.61	135.83	82.68	22.39	0.42923	150.75	3.692

Appendix B. Deduction of Model A

Fig. 6 (a) is assumed to establish the new composite model of elastic modulus for microstructure containing cubic precipitates. The goal of this section is to deduce the entire elastic modulus of Model A, E_A, shown in Fig. 6 (a) in a function of the elastic modulus of γ phase, γ′ phase, and volume fraction of γ′ phase. Fig. 6 (a) is a unit cell model of γ/γ′ microstructure, containing 1/8 cubic γ′ precipitates surrounded by γ matrix channels. This unit cell has "b" edge length of the cell and "a" edge length of γ′ precipitates. In this situation, γ′ volume fraction $V_{\gamma'}$ in the unit cell is defined by $V_{\gamma'} = \left(\frac{a}{b}\right)^3 = x^3$. In this situation, to deduce overall elastic modulus E_A, Model A is divided into two parts: Part A-1 shown in Fig. 6 (b) and Part A-2 shown in Fig. 6 (c).

B.1 Balance of elongation

To deduce the Model A easily, we assume environment with uniaxial external stress σ_{ext} to the unit cell shown in Fig. 6 (a). In this case, elongation of Model A toward stress direction is $e_A = \frac{\sigma_{ext}}{E_A}\cdot b$. If Model A is divided into two separated parts shown in Fig. 6, the same external stress is applied to Part A-1 and Part A-2, respectively. In this case, elongation of Part A-1 and Part A-2 is written in equation (B1) and equation (B2).

$$e_{A-1} = \frac{\sigma_{ext}}{E_{A-1}}\cdot(b-a) = \frac{\sigma_{ext}}{E_\gamma}\cdot(b-a) \tag{B1}$$

$$e_{A-2} = \frac{\sigma_{ext}}{E_{A-2}}\cdot a \tag{B2}$$

Therefore, a relation shown in equation (B3) has to be established based on balance of elongation.

$$e_A = e_{A-1} + e_{A-2} \tag{B3}$$

For this, E_{A-2} must be deduced in a function of elastic modulus of γ and γ′ phases and γ′ volume fraction.

B.2 Constrain condition to deduce E_{A-2}

The unit cell has to be an unit cell of microstructure under the load. Since the elastic moduli of γ and γ′ phases differ each other, external stress to each phase in Part A-2 is modulated so that the elongation of each region shows the same value. $\sigma_{ext}\cdot b^2 = \sigma_{\gamma'}\cdot a^2 + \sigma_\gamma\cdot\left(b^2 - a^2\right)$ relation exists so that each part satisfies the stress balance. In another form, this equation is written as $E_{A-2}\cdot\varepsilon_{A-2}\cdot b^2 = E_{\gamma'}\cdot\varepsilon_{\gamma'}\cdot a^2 + E_\gamma\cdot\varepsilon_\gamma\cdot\left(b^2 - a^2\right)$, using Hoock's low. At this time, constrain condition of the elongation of each part is applied so that elongation is the same in entire region of Part A-2, as following: $\varepsilon_{A-2} = \varepsilon_{\gamma'} = \varepsilon_\gamma$. Using these relations, entire elastic modulus of Part A-2 is formulated as following.

$$E_{A-2} = E_{\gamma'}\cdot x^2 + E_\gamma\cdot\left(1 - x^2\right) \tag{A4}$$

Therefore, elongation of Part A-2 can be written in equation (B5), using Hoock's law.

$$e_{A-2} = a\cdot\varepsilon_{A-2} = \frac{a\cdot\sigma_{ext}}{E_{\gamma'}\cdot x^2 + E_\gamma\cdot(1-x^2)} \tag{B5}$$

B.3 Unification of equations to elongation balance

Using equations shown above, elastic modulus of Model A by solving equation (B3) can be deduced as following.

$$E_A = \frac{\left((1-x^2)\cdot E_\gamma + x^2\cdot E_{\gamma'}\right)\cdot E_\gamma}{(1-x)\cdot\left((1-x^2)\cdot E_\gamma + x^2\cdot E_{\gamma'}\right) + x\cdot E_\gamma} \tag{B5}$$

Equation (B5) is longitudinal elastic modulus deduced by the role of mixture. This equation can be used for other elastic modulus, as in the cases of other mixture models [37]. Equation (A5) is identical to equation (9) in main text.

Equation (B5) can be solved by γ′ volume fraction x as following, and then, γ′ volume fraction of two phases alloy can be estimated using experimental elastic modulus data of the individual phases and alloy with two phases.

$$-x^2 \cdot \left(E_A \cdot \left(E_{\gamma'} - E_\gamma\right)\right) + x^2 \cdot \left(E_A - E_\gamma\right) \cdot \left(E_{\gamma'} - E_\gamma\right) + E_\gamma \cdot \left(E_A - E_\gamma\right) = 0 \tag{B6}$$

Appendix C. Comparison of the elastic modulus among conventional alloys

Elastic modulus of conventional alloys is shown in Fig. C1. Additionally, compositions of referenced alloys are also shown in Table C1.

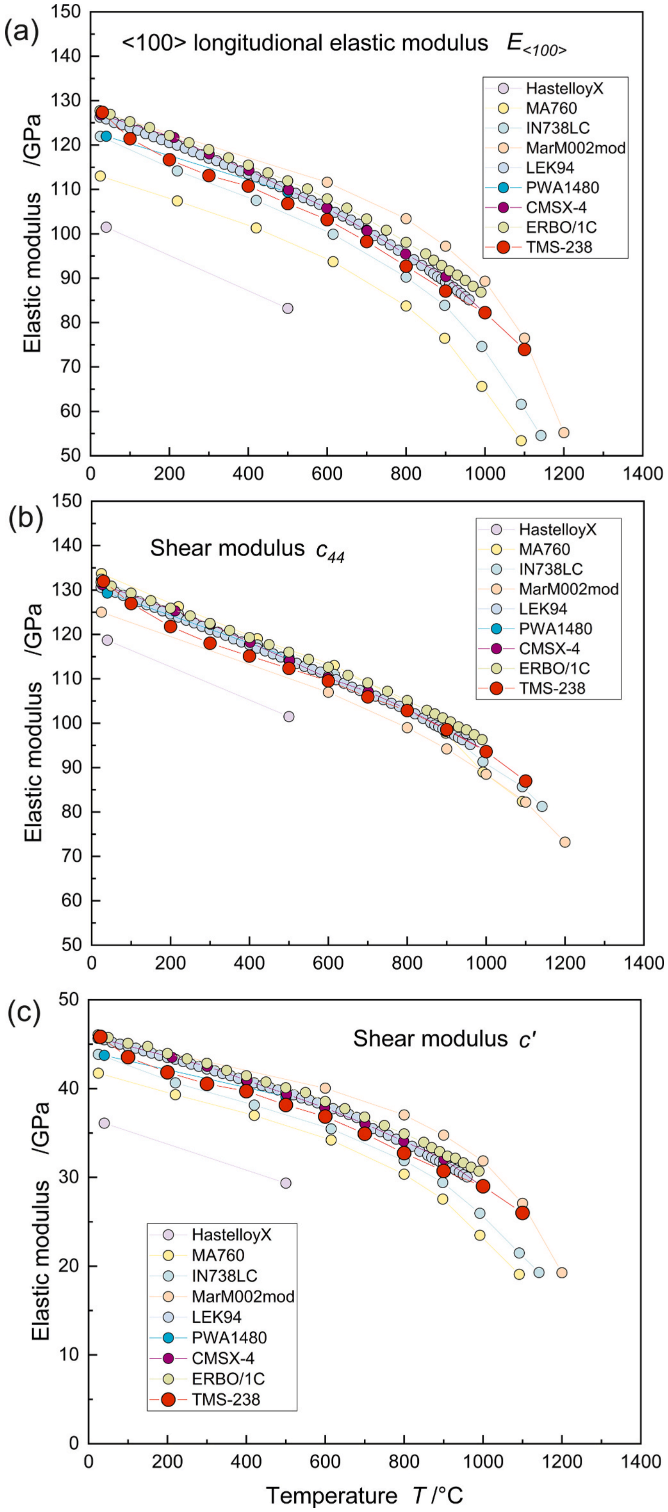

Fig. B1. Elastic modulus of conventional alloys. (a) <100> longitudinal elastic modulus, (b) shear modulus c_{44}, and (c) shear modulus c′.

Table C1
Compositions of referenced alloys in Fig. C1 (wt.%, Ni:bal.)

Alloys	Fe	Co	Cr	Mo	W	Al	Ti	Nb	Ta	Re	Ru	Y_2O_3	C	Hf	Method	Remark	Ref.
HastelloyX	18.5	1.5	22.0	9.0	0.6	–	–	–	–	–	–	–	0.10	–	Acoustic resonance	Solid solution alloy	[61]
MA760	1.2	–	19.4	1.9	3.4	5.9	–	–	–	–	–	1.04	0.04	–	Rod resonance	ODS alloy	[62]
IN738LC	0.1	8.6	16.0	1.8	2.7	3.4	3.4	0.9	1.9	–	–	–	0.11	–	Rod resonance	DS alloy	[62]
MarM002mod	–	10.0	9.0	–	10.0	5.5	1.2	–	2.5	–	–	–	0.15	1.5	Rod resonance	1st gen. SX alloy	[40]
PWA1480	–	5.0	10.0	–	4.0	5.0	1.5	–	12.0	–	–	–	–	–	Acoustic resonance	1st gen. SX alloy	[61]
LEK94	–	7.5	6.0	2.1	3.5	6.5	1.0		2.3	2.5	–	–	–	–	RPR	2nd gen. SX alloy	[63,64]
CMSX-4		9.6	6.4	0.6	6.4	5.6	1.0	–	6.5	3.0	–	–	–	–	Acoustic resonance	2nd gen. SX alloy	[36]
ERBO/1C	–	9.3	6.1	0.6	6.3	5.7	1.0	–	6.8	2.9	–	–	–	–	RPR	2nd gen. SX alloy	[63,64]
TMS-238	–	6.5	4.6	1.1	4.0	5.9	–	–	7.6	6.4	5.0	–	–	0.10	RPR	6th gen. SX alloy	This work

Data availability

Data will be made available on request.

References

[1] R.C. Reed, The Superalloys: Fundamentals and Applications, Cambridge University Press, 2008.

[2] M. Durand-Charre, The Microstructure of Superalloys, CRC Press, Florida, 1997.

[3] T.M. Pollock, S. Tin, Nickel-based superalloys for advanced turbine engines: chemistry, microstructure and properties, J. Propul. Power 22 (2006) 361–374, https://doi.org/10.2514/1.18239.

[4] T. Murakumo, Y. Koizumi, K. Kobayashi, H. Harada, Creep strength of Ni-base single-crystal superalloys on the γ/γ' tie-line, in: Proceedings of the 10th International Symposium on Superalloys, 2004, pp. 155–162, https://doi.org/10.7449/2004/Superalloys_2004_155_162.

[5] T. Murakumo, T. Kobayashi, Y. Koizumi, H. Harada, Creep behaviour of Ni-base single-crystal superalloys with various γ' volume fraction, Acta Mater. 52 (2004) 3737–3744, https://doi.org/10.1016/j.actamat.2004.04.028.

[6] Y. Ro, Y. Koizumi, H. Harada, High temperature tensile properties of a series of nickel-base superalloys on a γ/γ'tie line, Mater. Sci. Eng. A 223 (1997) 59–63, https://doi.org/10.1016/S0921-5093(96)10504-9.

[7] M.A. Ali, O. Shchyglo, M. Stricker, I. Steinbach, Coherency loss marking the onset of degradation in high temperature creep of superalloys: phase-field simulation coupled to strain gradient crystal plasticity, Comput. Mater. Sci. 220 (2023) 112069, https://doi.org/10.1016/j.commatsci.2023.112069.

[8] M.A. Ali, J.V. Görler, I. Steinbach, Role of coherency loss on rafting behavior of Ni-based superalloys, Comput. Mater. Sci. 171 (2020) 109279, https://doi.org/10.1016/j.commatsci.2019.109279.

[9] T.M. Pollock, A.S. Argon, Creep resistance of CMSX-3 nickel base superalloy single crystals, Acta Metall. Mater. 40 (1992) 1–30, https://doi.org/10.1016/0956-7151(92)90195-K.

[10] T.M. Pollock, A.S. Argon, Directional coarsening in nickel-base single crystals with high volume fractions of coherent precipitates, Acta Metall. Mater. 42 (1994) 1859–1874, https://doi.org/10.1016/0956-7151(94)90011-6.

[11] L.A. Jacome, P. Nörtershäuser, J.-K. Heyer, A. Lahni, J. Frenzel, A. Dlouhy, C. Somsen, G. Eggeler, High-temperature and low-stress creep anisotropy of single-crystal superalloys, Acta Mater. 61 (2013) 2926–2943, https://doi.org/10.1016/j.actamat.2013.01.052.

[12] T. Kobayashi, H. Harada, J. Zhang, Influence of heat treatment on microstructure and mechanical properties of 1st generation single-crystal superalloy, J. Japan Inst. Metals 70 (2006) 47–50, https://doi.org/10.2320/jinstmet.70.47.

[13] D.D. Pearson, F.D. Lemkey, B.H. Kear, Stress coarsening of gamma-prime and its influence on creep properties of a single crystal superalloy, in: Proceedings of the 4th International Symposium on Superalloys, American Society for Metals, Seven Springs Mountain Resort, 1980, pp. 513–520, https://doi.org/10.7449/1980/Superalloys_1980_513_520.

[14] M. Kamaraj, C. Mayr, M. Kolbe, G. Eggeler, On the influence of stress state on rafting in the single crystal superalloy CMSX-6 under conditions of high temperature and low stress creep, Scr. Mater. 38 (1998) 589–594, https://doi.org/10.1016/S1359-6462(97)00520-4.

[15] K. Serin, G. Göbenli, G. Eggeler, On the influence of stress state, stress level and temperature on γ-channel widening in the single crystal superalloy CMSX-4, Mater. Sci. Eng., A 387 (2004) 133–137, https://doi.org/10.1016/j.msea.2004.01.114.

[16] M. Kamaraj, K. Serin, M. Kolbe, G. Eggeler, Influence of stress state on the kinetics of γ-channel widening during high temperature and low stress creep of the single crystal superalloy CMSX-4, Mater. Sci. Eng., A 319–321 (2001) 796–799, https://doi.org/10.1016/S0921-5093(01)00950-9.

[17] N. Zhou, C. Shen, P. Sarosi, M. Mills, T. Pollock, Y. Wang, γ' rafting in single crystal blade alloys: a simulation study, Mater. Sci. Technol. 25 (2009) 205–212, https://doi.org/10.1179/174328408X361472.

[18] J.K. Tien, S.M. Copley, The effect of uniaxial stress on the periodic morphology of coherent gamma prime precipitates in nickel-base superalloy crystals, Matall. Trans. 2 (1971) 215–219, https://doi.org/10.1007/BF02662660.

[19] J. Buffiere, M. Ignat, A dislocation based criterion for the raft formation in nickel-based superalloys single crystals, Acta Metall. Mater. 43 (1995) 1791–1797, https://doi.org/10.1016/0956-7151(94)00432-H.

[20] F.R. Nabarro, Rafting in superalloys, Metall. Mater. Trans. 27 (1996) 513–530, https://doi.org/10.1007/BF02648942.

[21] M. Kamaraj, Rafting in single crystal nickel-base superalloys—An overview, Sadhana 28 (2003) 115–128, https://doi.org/10.1007/BF02717129.

[22] S. Socrate, D.M. Parks, Numerical determination of the elastic driving force for directional coarsening in Ni-superalloys, Acta Metall. Mater. 41 (1993) 2185–2209, https://doi.org/10.1016/0956-7151(93)90389-A.

[23] T. Ichitsubo, D. Koumoto, M. Hirao, K. Tanaka, M. Osawa, T. Yokokawa, H. Harada, Rafting mechanism for Ni-base superalloy under external stress: elastic or elastic–plastic phenomena? Acta Mater. 51 (2003) 4033–4044, https://doi.org/10.1016/S1359-6454(03)00224-6.

[24] J.C. Wang, M. Osawa, T. Yokokawa, H. Harada, M. Enomoto, Modeling the microstructural evolution of Ni-base superalloys by phase field method combined with CALPHAD and CVM, Comput. Mater. Sci. 39 (2007) 871–879, https://doi.org/10.1016/j.commatsci.2006.10.014.

[25] A. Gaubert, Y. Le Bouar, A. Finel, Coupling phase field and viscoplasticity to study rafting in Ni-based superalloys, Philos. Mag. 90 (2010) 375–404, https://doi.org/10.1080/14786430902877802.

[26] I.L. Svetlov, B.A. Golovko, A.I. Epishin, N.P. Abalakin, Diffusional mechanism of γ'-phase particles coalescence in single crystals of nickel-base superalloys, Scripta Metall. Mater. 26 (1992) 1353–1358, https://doi.org/10.1016/0956-716X(92)90648-X.

[27] P. Kontis, Z. Li, D.M. Collins, J. Cormier, D. Raabe, B. Gault, The effect of chromium and cobalt segregation at dislocations on nickel-based superalloys, Scr. Mater. 145 (2018) 76–80, https://doi.org/10.1016/j.scriptamat.2017.10.005.

[28] J.X. Zhang, T. Murakumo, Y. Koizumi, H. Harada, The influence of interfacial dislocation arrangements in a fourth generation single crystal TMS-138 superalloy on creep properties, J. Mater. Sci. 38 (2003) 4883–4888, https://doi.org/10.1023/B:JMSC.0000004409.70156.6a.

[29] T. Saito, H. Harada, T. Abe, H. Murakami, CALPHAD approach for prediction of local phase transformation at superlattice stacking fault in gamma prime precipitates in superalloys with multi-component system, Next Mater. 7 (2025) 100363, https://doi.org/10.1016/j.nxmate.2024.100363.

[30] T. Saito, M. Yuyama, H. Murakami, Effect of cobalt presence on creep properties of Ni-based single crystal superalloys at intermediate temperature, J. Alloys Compd. 1022 (2025) 179871, https://doi.org/10.1016/j.jallcom.2025.179871.

[31] J.X. Zhang, T. Murakumo, Y. Koizumi, T. Kobayashi, H. Harada, S. Masaki, Interfacial dislocation networks strengthening a fourth-generation single-crystal TMS-138 superalloy, Metall. Mater. Trans. A 33 (2002) 3741–3746, https://doi.org/10.1007/s11661-002-0246-7.

[32] M.V. Nathal, R.A. Mackay, The stability of lamellar γ-γ' structures, Mater. Sci. Eng. 85 (1987) 127–138, https://doi.org/10.1016/0025-5416(87)90474-5.

[33] T. Saito, H. Harada, T. Yokokawa, M. Osawa, K. Kawagishi, S. Suzuki, Effect of the interfacial strain anisotropy on the raft structure of Ni-Base single crystal superalloys and novel alloy design approach by controlling the lattice misfit and the elastic misfit, in: Proceedings of the 15th International Symposium on Superalloys, Springer Nature Switzerland, Seven Springs Mountain Resort, 2024, pp. 156–165, https://doi.org/10.1007/978-3-031-63937-1_15.

[34] T. Saito, H. Harada, T. Yokokawa, M. Osawa, K. Kawagishi, S. Suzuki, Raft structure of nickel base single-crystal superalloys, Mater. Trans. 65 (2024) 1443–1457, https://doi.org/10.2320/matertrans.MT-M2024081.

[35] T. Saito, M. Osawa, T. Yokokawa, H. Harada, T. Kobayashi, K. Kawagishi, S. Suzuki, Equations to predict the elastic modulus of the individual gamma and gamma-prime phases in multi-component Ni-base superalloys, in: Proceedings of the 14th International Symposium on Superalloys, Springer, Seven Springs Mountain Resort, 2020, pp. 312–323, https://doi.org/10.1007/978-3-030-51834-9_30.

[36] D. Siebörger, H. Knake, U. Glatzel, Temperature dependence of the elastic moduli of the nickel-base superalloy CMSX-4 and its isolated phases, Mater. Sci. Eng. A 298 (2001) 26–33, https://doi.org/10.1016/S0921-5093(00)01318-6.

[37] M. Fahrmann, W. Hermann, E. Fahrmann, A. Boegli, T.M. Pollock, H.G. Sockel, Determination of matrix and precipitate elastic constants in (γ-γ') Ni-base model alloys, and their relevance to rafting, Mater. Sci. Eng. A 260 (1999) 212–221, https://doi.org/10.1016/S0921-5093(98)00953-8.

[38] A. Epishin, B. Fedelich, M. Finn, G. Künecke, B. Rehmer, G. Nolze, C. Leistner, N. Petrushin, I. Svetlov, Investigation of elastic properties of the single-crystal nickel-base superalloy CMSX-4 in the temperature interval between room temperature and 1300° C, Crystals 11 (2021) 152, https://doi.org/10.3390/cryst11020152.

[39] A.I. Epishin, D.S. Lisovenko, Comparison of isothermal and adiabatic elasticity characteristics of the single crystal nickel-based superalloy CMSX-4 in the temperature range between room temperature and 1300°C, Mech. Solid. 58 (2023) 1587–1598, https://doi.org/10.3103/S0025654423601301.

[40] H. Kuhn, H. Sockel, Contributions of the different phases of two nickel-base superalloys to the elastic behaviour in a wide temperature range, Phys. Status Solidi 119 (1990) 93–105, https://doi.org/10.1002/pssa.2211190112.

[41] M. Enomoto, H. Harada, M. Yamazaki, Calculation of γ'/γ equilibrium phase compositions in nickel-base superalloys by cluster variation method, Calphad 15 (1991) 143–158, https://doi.org/10.1016/0364-5916(91)90013-A.

[42] O.M. Horst, D. Schmitz, J. Schreuer, P. Git, H. Wang, C. Körner, G. Eggeler, Thermoelastic properties and γ'-solvus temperatures of single-crystal Ni-base superalloys, J. Mater. Sci. 56 (2021) 7637–7658, https://doi.org/10.1007/s10853-020-05628-w.

[43] H. Harada, T. Ohno, T. Yamagata, T. Yokokawa, M. Yamazaki, Phase calculation and its use in alloy design program for nickel-base superalloys, in: Proceedings of the 6th International Symposium on Superalloys, Minerals, Metals & Materials Society, Seven Springs Mountain Resort, 1988, pp. 733–742, https://doi.org/10.7449/1988/SUPERALLOYS_1988_733_742.

[44] K. Kawagishi, A.-C. Yeh, T. Yokokawa, T. Kobayashi, Y. Koizumi, H. Harada, Development of an oxidation-resistant high-strength sixth-generation single-crystal superalloy TMS-238, in: Proceedings of the 12th International Symposium on Superalloys, Wiley-TMS, Seven Springs Mountain Resort, 2012, pp. 189–195, https://doi.org/10.1002/9781118516430.ch21.

[45] H.H. Demarest, Cube-resonance method to determine the elastic constants of solids, J. Acoust. Soc. Am. 49 (1971) 768–775, https://doi.org/10.1121/1.1912415.

[46] I. Ohno, Free vibration of a rectangular parallelepiped crystal and its application to detemination of elastic constants of orthorhombic crystals, J. Phys. Earth 24 (1976) 355–379, https://doi.org/10.4294/jpe1952.24.355.

[47] H. Yasuda, M. Koiwa, Determination of elastic constants of single crystals with cubic symmetry by the rectangular parallelepiped resonance method, J. Phys. Chem. Solids 52 (1991) 723–729, https://doi.org/10.1016/0022-3697(91)90174-X.

[48] H.H. Demarest, Cube-resonance method to determine the elastic constants of solids, J. Acoust. Soc. Am. 49 (1971) 768–775, https://doi.org/10.1121/1.1912415.

[49] A.B. Parsa, P. Wollgramm, H. Buck, C. Somsen, A. Kostka, I. Povstugar, P.-P. Choi, D. Raabe, A. Dlouhy, J. Müller, Advanced scale bridging microstructure analysis of single crystal Ni-base superalloys, Adv. Eng. Mater. 17 (2015) 216–230, https://doi.org/10.1002/adem.201400136.

[50] Y. Song, J. Fan, J. Li, H. Yang, R. Yuan, J. Yu, X. Ma, H. Kou, Z. Ren, J. Li, New insights into the optimisation of the solution heat treatment process and properties of CMSX-4 superalloys, Mater. Sci. Eng., A 890 (2024) 145947, https://doi.org/10.1016/j.msea.2023.145947.

[51] T. Saito, Y.-T. Chen, Y. Takata, K. Kawagishi, W.-C. Hsu, A.-C. Yeh, H. Murakami, Effect of heat treatments on microstructural evolution of a single crystal high entropy superalloy, Metals 10 (2020) 1600, https://doi.org/10.3390/met10121600.

[52] H. Okamoto, Al-Ni (aluminum-nickel), J. Phase Equil. 14 (1993) 257–259, https://doi.org/10.1007/BF02667823.

[53] Y. Mori, T. Yokokawa, T. Kobayashi, H. Harada, S. Suzuki, Phase stability of nickel-base single crystal superalloys containing iridium substituting for ruthenium, Mater. Trans. 57 (2016) 1845–1848, https://doi.org/10.2320/matertrans.MAW201606.

[54] R. Sowa, T. Goehler, L. Dankl, A. Kirzinger, A. Budziak, M. Parlinska-Wojtan, Microstructural stability of TMS-238$^{\mathrm{TM}}$ Ni-base superalloy during long-term exposure at high temperature, Mater. Sci. Technol. 37 (2021) 935–950, https://doi.org/10.1080/02670836.2021.1968583.

[55] C. Liu, W. Yang, J. Qin, P. Qu, H. Fu, Q. Wang, J. Zhang, L. Liu, Nucleation and transition sequences of TCP phases during heat-exposure in a Re-containing Ni-based single crystal superalloy, J. Mater. Sci. Technol. 202 (2024) 165–173, https://doi.org/10.1016/j.jmst.2024.02.081.

[56] K. Tanaka, M. Koiwa, Single-crystal elastic constants of intermetallic compounds, Intermetallics 4 (1996) S29–S39, https://doi.org/10.1016/0966-9795(96)00014-3.

[57] W. Voigt, Lehrbuch der Kristallphysik, Teubner-Verlag, Berlin, 1928.

[58] A. Reuss, Berechnung der Fließgrenze von Mischkristallen auf Grund der Plastizitätsbedingung für Einkristalle, J. Appl. Math. Mech. 9 (1929) 49–58, https://doi.org/10.1002/zamm.19290090104.

[59] S.V. Prikhodko, J.D. Carnes, D.G. Isaak, A.J. Ardell, Elastic constants of a Ni-12.69 at. % Al alloy from 295 to 1300 K, Scr. Mater. 38 (1997) 67–72, https://doi.org/10.1016/S1359-6462(97)00448-X.

[60] S.V. Prikhodko, H. Yang, A.J. Ardell, J.D. Carnes, D.G. Isaak, Temperature and composition dependence of the elastic constants of Ni3Al, Metall. Mater. Trans. A 30 (1999) 2403–2408, https://doi.org/10.1007/s11661-999-0248-9.

[61] H.A. Canistraro, E.H. Jordan, S. Shixiang, L.H. Favrow, F.A. Reed, Elastic constants of single crystal Hastelloy X at elevated temperatures, J. Eng. Mater. Technol. 120 (1998) 2420247, https://doi.org/10.1115/1.2812350.

[62] U. Bayerlein, H. Sockel, Determination of single crystal elastic constants from DS- and DR-Ni-based superalloys by a new regression method between 20C and 1200C, in: Proceedings of the 7th International Symposium on Superalloys, Warrendale, 1992, pp. 695–704, https://doi.org/10.7449/1992/Superalloys_1992_695_704.

[63] K. Demtröder, Einfluss von Chemismus und Mikrostruktur auf das Elastische Verhalten von Einkristallinen Nickelbasis Superlegierungen, Ruhr-University Bochum, Dissertation, 2019.

[64] K. Demtröder, G. Eggeler, J. Schreuer, Influence of microstructure on macroscopic elastic properties and thermal expansion of nickel-base superalloys ERBO/1 and LEK94, Mater. Werkst. 46 (2015) 563–576, https://doi.org/10.1002/mawe.201500406.